Lyman-alpha constraints on freeze-in and superWIMPs

Decant, Quentin

2022-03

Decant , Q , Heisig , J , Hooper , D C & Lopez-Honorez , L 2022 , ' Lyman-alpha constraints on freeze-in and superWIMPs ' , Journal of Cosmology and Astroparticle Physics , vol. 2022 , no. 3 , 041 . https://doi.org/10.1088/1475-7516/2022/03/041

http://hdl.handle.net/10138/351983
https://doi.org/10.1088/1475-7516/2022/03/041

Journal of Cosmology and Astroparticle Physics

SISSA

PAPER

Lyman-α constraints on freeze-in and superWIMPs

Journal of Cosmology and Astroparticle Physics
An IOP and SISSA journal

Lyman-α constraints on freeze-in and superWIMPs

Quentin Decant,[a] **Jan Heisig,**[b,c] **Deanna C. Hooper**[d] **and Laura Lopez-Honorez**[a,e]

[a]Service de Physique Théorique, CP225, Université Libre de Bruxelles, Bld du Triomphe, B-1050 Brussels, Belgium
[b]Institute for Theoretical Particle Physics and Cosmology, RWTH Aachen University, Sommerfeldstr. 16, D-52056 Aachen, Germany
[c]Centre for Cosmology, Particle Physics and Phenomenology (CP3), Université catholique de Louvain, B-1348 Louvain-la-Neuve, Belgium
[d]Department of Physics and Helsinki Institute of Physics, University of Helsinki, PL 64, FI-00014 Helsinki, Finland
[e]Theoretische Natuurkunde, Vrije Universiteit Brussel and The International Solvay Institutes, Pleinlaan 2, B-1050 Brussels, Belgium

E-mail: quentin.decant@ulb.be, heisig@physik.rwth-aachen.de, deanna.hooper@helsinki.fi, llopezho@ulb.be

Received November 25, 2021
Revised March 1, 2022
Accepted March 3, 2022
Published March 18, 2022

JCAP03(2022)041

 https://doi.org/10.1088/1475-7516/2022/03/041

Abstract. Dark matter (DM) from freeze-in or superWIMP production is well known to imprint non-cold DM signatures on cosmological observables. We derive constraints from Lyman-α forest observations for both cases, basing ourselves on a reinterpretation of the existing Lyman-α limits on thermal warm DM. We exclude DM masses below 15 keV for freeze-in, in good agreement with previous literature, and provide a generic lower mass bound for superWIMPs that depends on the mother particle decay width. Special emphasis is placed on the mixed scenario, where contributions from both freeze-in and superWIMP are similarly important. In this case, the imprint on cosmological observables can deviate significantly from thermal warm DM. Furthermore, we provide a modified version of the Boltzmann code CLASS, analytic expressions for the DM distributions, and fits to the DM transfer functions that account for both mechanisms of production. Moreover, we also derive generic constraints from $\Delta N_{\rm eff}$ measurements and show that they cannot compete with those arising from Lyman-α observations. For illustration, we apply the above generic limits to a coloured t-channel mediator DM model, in which case contributions from both freeze-in through scatterings and decays, as well as superWIMP production can be important. We map out the entire cosmologically viable parameter space, cornered by bounds from Lyman-α observations, the LHC, and Big Bang Nucleosynthesis.

Keywords: Lyman alpha forest, particle physics - cosmology connection, physics of the early universe, dark matter theory

ArXiv ePrint: 2111.09321

JCAP03(2022)041

Contents

1 Introduction

Cosmological observations imply that around 80% of the total matter content in our universe is made up of dark matter (DM) [1]. The gravitational impact of DM on the dynamics of visible matter has been measured on a large range of astrophysical and cosmological scales. Nonetheless, despite substantial effort, searches in colliders [2], direct [3], and indirect [4] experiments have so far not yielded any clear hints of interactions other than gravitational between the DM and the standard model particles.

While the aforementioned search strategies depend on the existence (and sufficient strength) of such an interaction, here we focus on a complementary path to constrain particle physics models of DM, by considering the DM imprint on the formation of cosmological structures and their potential contribution to the effective number of neutrinos, $\Delta N_{\rm eff}$. This is of particular relevance for very weakly interacting DM, potentially out-of-reach of other search strategies.

JCAP03(2022)041

An especially relevant probe in this direction is the Lyman-α forest, which provides a measurement of the positions of hydrogen clouds along the line-of-sight through the absorption lines of distant quasars [5–8]. Accordingly, Lyman-α forest observations probe structure on intermediate to small scales at redshifts around $2 \sim 6$ [9, 10]. These small-scale structures can be washed out by DM free-streaming, which is caused by significant deviations in the DM momentum distribution compared to the standard cold dark matter (CDM) scenario. Various groups have analysed data of the Lyman-α flux power spectrum [6–8, 11] and provided results for canonical warm dark matter (WDM), i.e. thermalised DM that freezes out relativistically in the early universe. In this scenario, masses below 5.3 keV [7] could be excluded under reasonable assumptions, see however [8] for a critical discussion of these assumptions, where the bound is then reduced to 1.9 keV.

Here we consider non-thermalised DM, i.e. a DM candidate that is so weakly coupled to the standard model that it never reaches thermal equilibrium with the primordial plasma of standard model particles. Such candidates are commonly referred to as *feebly interacting massive particles* (FIMPs). In these scenarios we can, therefore, no longer rely on the standard freeze-out mechanism to produce the correct relic abundance of DM. However, despite its feeble interaction, DM may still be produced to a sufficient amount by scatterings or decays of other (thermalised) particles. There are mainly two such production mechanisms that have been considered in the literature. *(i)* Freeze-in (FI) [12–18] is the non-efficient production of DM from decays or scatterings of particles in the thermal bath, where *non-efficient* refers to the fact that the respective production rate is small compared to the Hubble expansion rate. *(ii)* The superWIMP (SW) mechanism [19, 20] is the late decay of a frozen-out mother particle into DM. While both contributions may arise from the very same decay process, typically they take place at very different times. Hence, their characteristic momentum distribution — relevant for their imprint on cosmological structures — can be very different.

As the scales considered by Lyman-α data lie in the non-linear regime, normally assessing the impact of a certain DM model on the Lyman-α forest requires computationally expensive hydrodynamic simulations. However, on the basis of only the linear matter power spectrum — which we obtain from a modified version of the Boltzmann code CLASS [21, 22] — we can, to good approximation, use the results obtained for WDM to estimate Lyman-α constraints for the model considered here. To do so, we employ three different strategies, with varying degrees of sophistication and uncertainty. First, following the approach of [23], we consider the velocity dispersion as the characteristic measure of the free-streaming of DM. Second, we use an analytical fit to the transfer function, which relates the linear matter power spectrum of a model to a CDM one, and constrain the fitting parameters, as was done in [5, 24]. Finally, we make use of the area criterion [25, 26], which considers the integral over the one-dimensional linear power spectrum as a characteristic quantity constrained by Lyman-α data. Although all three methods will allow us to derive limits on the pure FI or SW case, only the latter enables the analysis of the mixed scenario. In our analyses, we also study the conditions under which the FIMPs considered here could give rise to significant contributions to $\Delta N_{\rm eff}$, reaching the conclusion that this is not expected to provide any more stringent constraints on the FI or SW scenarios.

Having derived general bounds for these models, we then consider a benchmark scenario with a top-philic simplified t-channel mediator model introducing a coloured scalar top-partner and a singled Majorana DM candidate, both odd under a discrete Z_2-symmetry that stabilises DM. We thereby extend the work of [27], where Lyman-α constraints on the model were estimated by simple considerations of the free-streaming length. Furthermore,

JCAP03(2022)041

following [28], we take into account important bound state formation effects in the freeze-out process of the mediator, which are particularly relevant for the computation of the Lyman-α constraints towards high mediator masses.

This paper is organised as follows. We begin in section 2 by discussing the different production mechanisms for FIMPs, as well as the corresponding Boltzmann equations. In section 3, we focus on the cosmological implications of FIMP DM, reviewing the observables that will constrain these models. We then focus on a specific realisation of our set-up, top-philic FIMPs, in section 4, before concluding in section 5. Finally, in appendix A we go into more detail about SW production, in App, B we provide all relevant expressions for Sommerfeld enhancement and bound state formation, and in appendix C we discuss the various approximations and consideration made to extract the Lyman-α bounds.

2 FIMPs in the early universe

To understand the production of FIMPs we first review the underlying formalism. The case of FIMP production from decays and scatterings and their impact on small-scale structures has already been addressed in several recent works [23, 29–32]. Nevertheless, here we briefly summarise the relevant steps of the computation and precise, where relevant, new inputs compared to previous literature. We also detail our implementation of FIMP momentum distribution functions in the public Boltzmann code CLASS.[1] Complementary discussion on the Boltzmann equations for FI can be found in e.g. [33, 34].

2.1 Boltzmann equations

In order to describe the momentum distribution of FIMPs, one has to solve the unintegrated Boltzmann equation for the DM phase-space distribution function $f_\chi(t,p)$

$$\frac{\mathrm{d}f_\chi}{\mathrm{d}t} = \mathcal{C}[f_\chi] \tag{2.1}$$

where χ refers to the DM particle, with t and p the proper time and momentum, and $\mathcal{C}$ refers to the collision terms responsible for FIMP production from the decays or scatterings of some mother particle B. The number density of any species i can be obtained by integrating out the distribution function $f_i(t,p)$ as

$$n_i = g_i \int \frac{\mathrm{d}^3p}{(2\pi)^3} f_i(t,p)\,, \tag{2.2}$$

where g_i is the number of degrees of freedom (dof) of the species i. It is usually appropriate to re-express proper time and momentum in terms of independent dimensionless variables. In the context of the DM studied here, the time variable t is traded with $x = m_{\rm ref}/T$, where $m_{\rm ref}$ denotes some reference mass (often the mass of the mother particle B for FIMP production) and T denotes the temperature of the standard model bath. The relation between x, or equivalently T, and t can be easily obtained when entropy is conserved, which we will assume throughout this work. In this case, we have $\mathrm{d}(sa^3)/\mathrm{d}t = 0$, where s is the entropy density and a the scale factor. As a result, keeping in mind that $s \propto g_{*S}T^3$, one obtains

$$\frac{\mathrm{d}\ln T}{\mathrm{d}\ln t} = -\bar{H} \quad \text{with} \quad \bar{H} = \frac{H}{1 + 1/3\,\mathrm{d}\ln g_{*S}/\mathrm{d}\ln T}\,, \tag{2.3}$$

[1] Our modified CLASS version can be found at https://github.com/dchooper/class_fisw.

JCAP03(2022)041

where $g_{*S}(T)$ denotes the number of relativistic dof in the thermal bath of temperature T contributing to the entropy, and $H = \mathrm{d}\ln a/\mathrm{d}t$ is the Hubble expansion rate. In a radiation dominated era, the Hubble rate reduces to

$$H = \frac{T^2}{M_0(T)} \quad \text{with} \quad M_0(T) = M_{\rm Pl}\sqrt{\frac{45}{4\pi^3 g_*(T)}}\,, \tag{2.4}$$

where $M_{\rm Pl} = 1.2 \times 10^{19}\,\mathrm{GeV}$ is the Planck mass and $g_*(T)$ denotes the number of relativistic dof in the thermal bath of temperature T, this time contributing to the radiation energy density.

Here we mostly consider scenarios for which $g_*(T), g_{*S}(T)$ are constant before FIMP production. As a result, $\frac{d\ln T}{d\ln t} = -H$ and it is convenient to use

$$x = \frac{m_B}{T} \quad \text{and} \quad q = \frac{p}{T} \tag{2.5}$$

as time and momentum-independent variables[2] and the Boltzmann equation from eq. (2.1) simply reduces to

$$xH\partial_x f_\chi = \mathcal{C}[f_\chi]\,. \tag{2.6}$$

In appendix A we discuss the relevant choice of time and momentum variable for time-varying g_*, g_{*S}.

We assume that the initial FIMP abundance is negligible. We use the compact notation $\mathrm{in} \to \mathrm{fin} + \chi$ for the DM particle χ production processes, including decays and scatterings. With "in" ("fin") we refer to an ensemble of initial (final) state particles as a source for DM production. In this context, the collision term in eq. (2.6) reads

$$\mathcal{C}[f_\chi] = \frac{1}{2g_\chi E_\chi}\int \Pi_\alpha \frac{\mathrm{d}^3 p_\alpha}{(2\pi)^3 2E_\alpha}(2\pi)^4\delta^4(P_{\rm fin} + p_\chi - P_{\rm in}) f_{\rm in}(1 \pm f_{\rm fin})(1 \pm f_\chi)|\mathcal{M}|^2_{\mathrm{in}\to\mathrm{fin}+\chi}\,. \tag{2.7}$$

In this expression the index α runs over all particles in the initial and final states except for DM, P_α is the sum of the four-momenta of initial or final state particles for $\alpha = $ in and fin, $f_{\rm in}$ refers to the product of the distribution functions of the initial state particles, and $(1 \pm f_{\rm fin})$ is the product of Pauli blocking (with a minus sign) or Bose-Einstein enhancing (with a plus sign) factors for final state particles. Furthermore, $|\mathcal{M}|^2_{\mathrm{in}\to\mathrm{fin}+\chi}$ denotes the amplitude squared *summed* over initial and final state quantum numbers. For concreteness, we will focus here on 2-body decays of the form $B \to A\chi$, and $2 \to 2$ scatterings of the form $BB' \to A'\chi$ for DM production. As such, we consider a scenario where B and χ are odd under a Z_2 symmetry that stabilizes DM. We will also neglect spin statistics effects by taking $(1 \pm f_{\rm fin}) = 1$, see e.g. [31, 32, 34] for some complementary studies.

In this paper we focus on scenarios in which the mother particle is in kinetic equilibrium while producing the DM and $m_B > m_\chi$. For B in kinetic equilibrium, its distribution function can be written as (see e.g. [35, 36] for a discussion)

$$f_B(x,q) = \frac{Y_B(x)}{Y_B^{\rm eq}(x)} f_B^{\rm eq}(x,q)\,, \tag{2.8}$$

where $f^{\rm eq}(x,q)$ denotes the usual equilibrium distribution function with zero chemical potential. In order to derive an analytic estimate for the DM distribution function, we will consider

[2] In full generality, $q = p/T$, which is not a time-independent variable as the temperature scales as $T \propto g_{*S}^{1/3} a^{-1}$ and $p \propto 1/a$.

JCAP03(2022)041

a Maxwell-Boltzmann distribution for B, but we have explicitly checked numerically that the results do not change significantly when considering e.g. a Bose-Einstein distribution, see also [29, 32, 33].

The average DM momentum at the time of production, and its subsequent redshifted value, provide a good tool to estimate the importance of cosmological constraints arising from small-scale structure, more specifically the Lyman-α power flux constraints and the number of extra relativistic dof, see e.g. [23, 29, 31, 32] and also e.g. [37] in a slightly different context. In particular, the rescaled n^{th}-moment of the distribution is obtained evaluating

$$\langle q^n \rangle = \frac{\int \mathrm{d}^3 q \, q^n f_\chi(q)}{\int \mathrm{d}^3 q \, f_\chi(q)} \,, \tag{2.9}$$

where $f_\chi(q)$ is the FIMP distribution after production ($\equiv f_\chi(x, q)$ for $x \gg x_{\text{prod}}$).

2.2 FIMPs from decays

For DM production through decays, the collision term in the Boltzmann eq. (2.6) reduces to

$$\mathcal{C}_{\text{dec}}[f_\chi] = \frac{x}{16\pi g_\chi q \sqrt{q^2 m_B^2 + m_\chi^2 x^2}} \int_{\xi_-}^{\xi_+} \mathrm{d}\xi_B f_B |\mathcal{M}|^2_{B\to A\chi} \,, \tag{2.10}$$

where $\xi_B = E_B/T$ and the values of $\xi_\pm$ are discussed in appendix A, see also [30]. In what follows, we distinguish between the FI and the SW production from decays of a mother particle that is in kinetic equilibrium with the thermal bath. In the case of FI production, discussed in section 2.2.1, the mother is both in kinetic and chemical equilibrium. On the other hand, SW production would refer to the DM production after B freeze-out, i.e. after B chemically decouples, see section 2.2.2. Accordingly, the two contributions — although stemming from the very same decay process — can arise at different times with distinct mean momenta and momentum distributions. This is illustrated in section 2.2.3. In this context, it is convenient to introduce the dimensionless ratio

$$R_\Gamma^{\text{prod}} = \frac{M_0(T_{\text{prod}})\Gamma_{B\to A\chi}}{m_B^2}, \tag{2.11}$$

where $M_0(T_{\text{prod}})$ corresponds to the rescaled Planck mass of eq. (2.4) with the number of relativistic dof estimated at the DM production temperature T_{prod}.

2.2.1 Freeze-in from decays

The largest contribution to DM freeze-in from decays of a bath particle B, arises around $x_{\text{FI}} = m_B/T \sim 3$ [18] due to the interplay of two competing effects. On the one hand, in a radiation dominated era, $\Gamma_{B\to A\chi}/H$ increases with x, leading the decay to become more efficient at late times. On the other hand, once the bath particle becomes non-relativistic, i.e. $x \gtrsim 1$, its number density starts to decrease exponentially.

Considering renormalisable interactions in the radiation dominated era and assuming[3] $m_\chi \ll m_B, m_A$ as well as a Maxwell-Boltzmann distribution for the mother bath particle B,

[3] If the DM mass is not neglected in the computation of the DM distribution function, a further analytic expression for the latter would be needed, while an expression for $\partial_x f_\chi$ is given in [30]. Integrating out the distribution function numerically, ref. [30] showed that the analytic form of f_χ obtained in the limit $m_\chi \to 0$, eq. (2.12), is a very good approximation in the range of q relevant to extract the Lyman-α constraints.

JCAP03(2022)041

i.e. $f_B = \exp(-E_B/T)$, we can obtain a simple analytic expression for f_χ of the form [23, 29]

$$g_\chi f_\chi^{\mathrm{FI,\,dec}}(q) = 2 g_B \frac{R_\Gamma^{\mathrm{FI}}}{\delta^3}\sqrt{\frac{\pi\delta}{q}}\exp\left(-\frac{q}{\delta}\right), \tag{2.12}$$

$$\text{with} \quad \delta = \frac{m_B^2 - m_A^2}{m_B^2} \tag{2.13}$$

where we use the short-hand notation $f_\chi^{\mathrm{FI,\,dec}}(q) = f_\chi^{\mathrm{FI,\,dec}}(x \to \infty, q)$. Furthermore, g_B is the number of dof of B, T_{FI} is the temperature at FI production, which is $T_{\mathrm{FI}} = m_B/x_{\mathrm{FI}}$. Further details on the computation and involved approximations are given in appendix A. Integrating out eq. (2.12) over momenta, one obtains the DM abundance from FI,

$$\Omega_\chi h^2|_{\mathrm{FI,\,dec}} = m_\chi \times \frac{135}{8\pi^3}\frac{g_B}{g_*\left(T_{\mathrm{FI}}\right)} R_\Gamma^{\mathrm{FI}} \frac{s_0 h^2}{\rho_{\mathrm{crit}}}, \tag{2.14}$$

where $\rho_{\mathrm{crit}} = 3M_{\mathrm{Pl}}^2 H_0^2/(8\pi)$ is the critical energy density, s_0 is the entropy density today, and h is the rescaled Hubble parameter today, $h = H_0/(100\,\mathrm{km\,s^{-1}Mpc^{-1}}) \sim 0.7$. Making use of eqs. (2.9) and (2.12), the n^{th}-moment of the rescaled DM momentum distribution of (2.12) is given by

$$\langle q^n\rangle|_{\mathrm{FI,\,dec}} = \frac{4}{3\sqrt{\pi}}\Gamma\left(\frac{5}{2}+n\right) \times \delta^n, \tag{2.15}$$

where the Γ denotes the mathematical Gamma-function. In particular, $\langle q\rangle|_{\mathrm{FI,\,dec}} = 5/2 \times \delta$ while for thermal WDM one would get $\langle q\rangle_{\mathrm{thermal}} \simeq 3$, see e.g. [29] for a discussion.

2.2.2 FIMPs from superWIMP mechanism

After the time at which B gets chemically decoupled, usually referred to as freeze-out time, around $x_{\mathrm{FO}} \sim 25$, the frozen out particle eventually decays into DM and, hence, provides a contribution to the DM abundance. This DM production mechanism is usually referred to as the SW mechanism. Interestingly, the associated DM phase-space distribution might also peak at significantly higher q values than in the case of FI production.

To get an analytic expression of the DM phase-space distribution, we employ the ansatz of eq. (2.8) for the bath particle distribution, together with the non-relativistic expression for the B equilibrium comoving density, $Y_B^{\mathrm{eq}}(x)$. After chemical decoupling only late B decays can affect the B abundance so that Y_B should satisfy

$$\frac{\mathrm{d}\ln Y_B}{\mathrm{d}x} = -R_\Gamma^{\mathrm{SW}} x \frac{K_1(x)}{K_2(x)} \quad \Rightarrow \quad Y_B(x) \simeq Y_{\mathrm{FO}} e^{-R_\Gamma^{\mathrm{SW}}(x^2 - x_{\mathrm{FO}}^2)/2} \quad [x > x_{\mathrm{FO}}], \tag{2.16}$$

where R_Γ^{SW} is given by eq. (2.11) with $M_0 = M_0(T_{\mathrm{SW}})$ and Y_{FO} is the roughly constant frozen-out bath particle abundance between B chemical decoupling and complete decay to DM at x_{SW}, i.e. $Y_B \simeq Y_{\mathrm{FO}}$ for $x_{\mathrm{FO}} \lesssim x \lesssim x_{\mathrm{SW}}$. In order to derive the above analytic expression we have further assumed that $K_1(x)/K_2(x) \simeq 1$ in the non-relativistic limit, as well as a constant number of relativistic dof. From eq. (2.16) it is clear that the characteristic temperature parameter at which the decay takes place is

$$x_{\mathrm{SW}} = \sqrt{\frac{2}{R_\Gamma^{\mathrm{SW}}}}. \tag{2.17}$$

JCAP03(2022)041

Plugging the above inputs into eq. (2.10) we can readily integrate over the ξ_B with the lower integration bound $\xi_{B\,\mathrm{min}} = q/\delta + \delta x^2/(4q)$ and get

$$g_\chi \partial_x f_\chi^{\mathrm{SW}}(x,q) = \frac{Y_B(x)}{Y_B^{\mathrm{eq}}(x)} \times \frac{g_B}{\delta}\frac{x^2}{q^2} R_\Gamma^{\mathrm{SW}} \exp\left(-q/\delta - \delta x^2/(4q)\right) . \tag{2.18}$$

Integrating eq. (2.18) over x we obtain

$$\begin{aligned} g_\chi f_\chi^{\mathrm{SW}}(q) &\simeq \sqrt{8\pi}\,\frac{C_{\mathrm{SW}}}{q\delta}\,\exp\left(-\frac{2R_\Gamma^{\mathrm{SW}} q^2}{\delta^2}\right) \\ \text{with} \quad C_{\mathrm{SW}} &= g_{*S}(x_{\mathrm{SW}}) Y_{\mathrm{FO}} \frac{R_\Gamma^{\mathrm{SW}}}{\delta}(2\pi)^{3/2}\frac{2\pi^2}{45} , \end{aligned} \tag{2.19}$$

where g_{*S} has to be evaluated at the temperature of SW decay. To derive such a simple expression, we have assumed that the relevant (x,q) parameter space for SW corresponds to $x \gg x_{\mathrm{FO}}$ and $2qR_\Gamma^{\mathrm{SW}} \ll \delta$, see appendix A for details. In addition, the results derived here assumed that g_{*S} is constant throughout SW production. While this is not always true, we have explicitly checked that when considering $g_{*S} = g_{*S}(x_{\mathrm{SW}})$ in eq. (2.19) the results are in very good agreement with numerical calculations taking a time-dependent g_{*S} into account, see the discussion in appendix A.[4] Finally, integrating out eq. (2.19) over momenta, we simply recover that the DM abundance arising from SW, Y_χ^{SW} is equal to Y_{FO}, confirming the consistency of our approach. We can also easily evaluate the n^{th}-moments of the DM rescaled momentum distribution (eq. (2.19)) from SW production, which reduces to

$$\langle q^n \rangle|_{\mathrm{SW}} \simeq \left(2R_\Gamma^{\mathrm{SW}}\right)^{-n/2} \delta^n\, \Gamma\left(\frac{n}{2}+1\right) . \tag{2.20}$$

In particular, for $n=1$, we have $\langle q \rangle|_{\mathrm{SW}} = \delta\sqrt{\frac{\pi}{8R_\Gamma^{\mathrm{SW}}}}$.

2.2.3 When superWIMP meets freeze-in

As mentioned above, one single decay process can give rise to two types of FIMP DM production mechanisms: one from FI and another from SW. In figure 1 we illustrate the comoving number densities evolution as a function of the temperature parameter x (left), and the DM distribution function $f_\chi(q)$ dependency in rescaled momentum (right) for two benchmarks taking $R_\Gamma = 7\times10^{-4}$ (green curves) and $R_\Gamma = 7\times10^{-8}$ (purple curves). We have assumed $m_B \gg m_A$, such that $\delta = 1$ and $g_* = g_{*,S} = 106.75$ at both T_{FI} and T_{SW}, i.e. $R_\Gamma = R_\Gamma^{\mathrm{FI}} = R_\Gamma^{\mathrm{SW}}$.

In the left panel of figure 1, we show both $Y_B(x)$, the bath particle comoving abundance (dashed lines), and $Y_\chi(x)$, the DM comoving abundance (solid lines). At early times, Y_B follows the equilibrium Maxwell-Boltzmann distribution which is already becoming exponentially suppressed around $x \sim 1$. At chemical decoupling, for $x = x_{\mathrm{FO}}$, Y_B freezes-out and remains constant, with $Y_B = Y_{\mathrm{FO}}$, up until $x \sim x_{\mathrm{SW}}$ where it fully decays to DM. In parallel, the DM abundance is slowly produced up until $x_{\mathrm{FI}} \sim 3$ where it freezes in at a value $Y_\chi(x_{\mathrm{FI}})$. The second contribution to the DM abundance from the SW mechanism is produced around $x_{\mathrm{SW}} \sim 53$ and 5.3×10^4 for $R_\Gamma = 7\times10^{-4}$ and $R_\Gamma = 7\times10^{-8}$, respectively, contributing

[4] Notice that in [38, 39], B has been assumed to be kinetically decoupled since freeze-out time, i.e. eq. (2.8) does not hold. This is usually not the case when B is charged under standard model gauge group, which we assume here. Therefore, we cannot directly compare our results to theirs.

JCAP03(2022)041

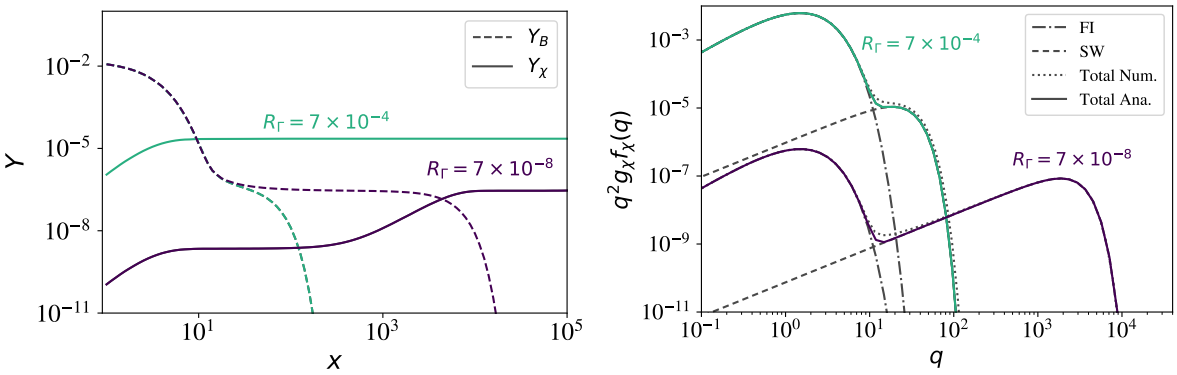

Figure 1. FIMP production from B decays with B in kinetic equilibrium with the standard model bath. Two benchmarks are displayed taking $R_\Gamma = 7 \times 10^{-4}$ (green curves) and $R_\Gamma = 7 \times 10^{-8}$ (purple curves). *Left:* bath particle (dashed curves) and DM (solid curves) comoving number density as a function of the time variable x. *Right:* FIMP distribution function multiplied by the momentum squared, $q^2 g_\chi f_\chi(q)$, as a function of the rescaled momentum q. The analytic FI and SW contributions are shown with grey dashed and dot dashed curves respectively while the coloured solid lines correspond to the sum of the latter two. With the grey dotted curves we also show the results obtained by integrating eq. (2.10) without any approximation.

around 2 % and 99% to the relic DM abundance. If $Y_B(x_{\rm FO})$ is large enough compared to $Y_\chi(x_{\rm FI})$, the SW contribution can significantly affect the DM abundance, as visible for $R_\Gamma = 7 \times 10^{-8}$ (purple curve).

In the right panel of figure 1, we show the DM distribution multiplied by the rescaled momentum squared, $q^2 g_\chi f_\chi(q)$, as a function of q. The FI from B decay contribution to $f_\chi(q)$, as in eq. (2.12), is shown with grey dot dashed curves while the SW contribution from eq. (2.19) is shown with dashed curves. The sum of the latter two analytic results is shown with coloured solid curves. For comparison, we show with grey dotted curves the numerical result obtained integrating out the collision term of eq. (2.10) without any approximations. We see that both coloured and grey dotted lines give rise to very similar results. More quantitatively, for $R_\Gamma = 7 \times 10^{-4}$ (7×10^{-8}) we introduce a relative error below 1% (around 2%) in estimating the DM relic abundance by integrating out the analytic result instead of the numeric result. This, in particular, illustrates that the analytic results derived in the previous section provide a very good estimate of the SW contribution to DM abundance and distribution function. From this figure, it is also clear that the FI through decay distribution peaks around $q \sim \mathcal{O}(1)$ as expected from eq. (2.15) while the SW distribution is always expected to peak at larger q values giving rise to a multimodal DM distribution.

As a final comment, let us also mention that while here we illustrate the case where FI and SW contributions arise from the same mother particle, B, the most relevant contribution to each production mechanism could also originate from two different particles, see e.g. [39].

2.3 FIMPs from scatterings

FIMPs could also have been produced in the early universe through FI from scatterings. In the case of $BB' \to A'\chi$ scatterings, assuming a Maxwell-Boltzmann distributions for the

JCAP03(2022)041

bath particles B and B', we have[5]

$$\mathcal{C}_{\rm scat}[f_\chi] = \frac{1}{32\pi^2 g_\chi E p}\int_{s_{\rm min}} {\rm d}s \int_{E_{A'}^{\rm min}} {\rm d}E_{A'}\, \exp\left(-\frac{E+E_{A'}}{T}\right)\frac{\hat{\sigma}}{2}\frac{s}{\sqrt{(p\cdot p_{A'})^2-(m_\chi m_{A'})^2}}\,, \tag{2.21}$$

where $\hat{\sigma}(s)$ denotes the reduced $BB' \to A'\chi$ cross-section, which is a function of the centre of mass energy squared s, satisfying

$$\frac{{\rm d}\hat{\sigma}}{{\rm d}t} = \frac{1}{8\pi s}|\mathcal{M}|^2\,, \tag{2.22}$$

where the derivative is taken with respect to the Mandelstam variable t, and $|\mathcal{M}|^2$ is again the transition amplitude squared summed over initial and final state dof. Going to the limit of $m_\chi \ll m'_A, m_B, m'_B$, eq. (2.21) reduces to

$$g_\chi f_\chi^{\rm FI,\,scat}(q) = \frac{1}{32\pi^2 q^2}\frac{M_0^{\rm FI}}{m_{\rm ref}}\int_0^\infty {\rm d}x \int_{\tilde{s}_{\rm min}}^\infty {\rm d}\tilde{s}\frac{\hat{\sigma}\tilde{s}}{\tilde{\Delta}}\exp\left(-\frac{q\tilde{s}}{\tilde{\Delta}}-\frac{\tilde{\Delta}}{4q}\right) \tag{2.23}$$

$$\text{with}\quad \Delta = s - m_{A'}^2 \quad\text{and}\quad \tilde{\Delta} = \Delta/T^2\,, \tag{2.24}$$

where we again use the short-hand notation $f_\chi^{\rm scat}(q) = f_\chi^{\rm FI,\,scat}(x\to\infty, q)$, which is the FIMP distribution today when produced through $2\to 2$ scatterings, in agreement with [29]. In eq. (2.23), we denote with a tilde dimensionless variables rescaled with temperature with e.g. $\tilde{s} = s/T^2$.

As the details of the distribution function from FI through scatterings is quite model-dependent, see e.g. [23], we leave for section 4 a more thorough discussion on the latter in the context of a top-philic DM scenario. Nevertheless, when $s_{\rm min}$ and $\hat{\sigma}$ can be assumed to be temperature-independent, it is possible to get a generic expression for $\langle q^n\rangle$ from eq. (2.9), namely

$$\langle q^n\rangle|_{\rm FI,\,scat} = \frac{4}{3\sqrt{\pi}}\Gamma\left(\frac{5}{2}+n\right)\times\left[1+\frac{\int {\rm d}s\,\hat{\sigma}\left(-1+\left(1-m_{A'}^2/s\right)^n\right)/s^{3/2}}{\int {\rm d}s\,\hat{\sigma}/s^{3/2}}\right]\,, \tag{2.25}$$

where the integrals over s run from $s_{\rm min} = \max\left((m_B+m_{B'})^2, m_{A'}^2\right)$ to ∞.[6] The overall prefactor is nothing but $\langle q^n\rangle|_{\rm FI,\,dec}$ in the $\delta = 1$ case. In addition, the second term in the squared parenthesis vanishes when $m_{A'}$ is small with respect to one of the masses of the initial bath particles. Therefore, it is apparent that, when there is one initial state particle that is much heavier than the final state particles, the squared parenthesis in eq. (2.25) reduces to 1, and we recover the FI through decay result. This in particular implies that FI through decay and scattering distributions share the same q-dependence,

$$f_\chi(q)|_{\rm FI,\,scat} \propto q^{-1/2}\exp(-q)\,, \qquad [m_{A'}, m_\chi \ll m_B \text{ or } m_{B'}]\,, \tag{2.26}$$

[5] In eq. (2.21), we have an extra factor of 1/2 compared to [29], which we believe to be a typo, as our numerical integration fully agrees with the results of [23].

[6] In general, in eq. (2.23), the lower integration limit on the centre of mass energy squared and the reduced cross-section could be explicit functions of the bath temperature, i.e. $s_{\rm min} = s_{\rm min}(T)$ and $\hat{\sigma} = \hat{\sigma}(s,T)$. This is, for example, the case when taking into account thermal corrections such as a temperature-dependent mass. In that case the results and implications of eqs. (2.25) and (2.28) do not apply.

JCAP03(2022)041

which would agree with the distributions used in [32]. Even when $m_{A'}$ is non-negligible, since $m_{A'}^2 \leq s_{\rm min}$, the second term in the squared parenthesis is always negative. We thus find that

$$\langle q^n \rangle|_{\rm FI,\,scat} \leq \frac{4}{3\sqrt{\pi}}\Gamma\left(\frac{5}{2}+n\right) \tag{2.27}$$

both for FI from scatterings and from decays. Finally, the contribution to the relic density from FI through scattering is given by

$$\Omega_\chi h^2|_{\rm FI,\,scat} = m_\chi \times \frac{s_0}{\rho_{\rm crit}/h^2}\frac{135 M_0}{256\pi^5 g_*(T_{\rm FI})} \times \left(\int_{s_{\rm min}}^\infty {\rm d}s\, \frac{\hat{\sigma}}{s^{3/2}}\right), \tag{2.28}$$

assuming again that $s_{\rm min}$ and $\hat{\sigma}$ are temperature-independent.

2.4 FIMP distribution functions in class

In order to precisely follow the cosmological evolution of the FIMPs, we have implemented the FIMP distribution functions in the public Boltzmann code CLASS [22]. For that purpose, it is convenient to introduce a new rescaled momentum variable,

$$q_\star = \frac{p(t)}{T_\star(t)} \quad \text{with} \quad T_\star(t) = c_\star T_\gamma(t_{\rm prod})\frac{a_{\rm prod}}{a(t)} \tag{2.29}$$

where $p \propto 1/a$ is the proper momentum, $c_\star$ is a constant factor that will be chosen for each FIMP production mode, $a_{\rm prod}$ and $T_\gamma(t_{\rm prod})$ are the scale factor and the photon temperature at the time of production. The definition of $T_\star(t)$ is introduced in CLASS through the input variable `T_ncdm` which corresponds to the ratio of temperatures $T_\star$ and T_γ today. Using eq. (2.29), the latter dimensionless variable takes the form

$$\texttt{T\_ncdm} = \frac{T_\star(t_0)}{T_\gamma(t_0)} = c_\star a_{\rm prod}\frac{T_\gamma(t_{\rm prod})}{T_\gamma(t_0)} = c_\star\left(\frac{g_{*S}(t_0)}{g_{*S}(t_{\rm prod})}\right)^{1/3}, \tag{2.30}$$

where t_0 refers to the time today, the scale factor today is $a_0 = 1$ and $g_{*S}(t_0) = 3.91$. We see that `T_ncdm` reduces to the ratio of relativistic dof at production time and today to the power $1/3$ up to the constant prefactor $c_\star$, see e.g. [22, 31] for other NCDM models.

In practice, for our implementation of FI and SW in CLASS, we have chosen the $c_\star$ prefactors in eq. (2.30) to be $c_\star^{\rm FI} = \delta$ and $c_\star^{\rm SW} = \delta/\sqrt{2R_\Gamma^{\rm SW}}$. This implies that the distribution functions for FI from decay and SW of eqs. (2.12) and (2.19) take the following simpler forms:

$$\begin{cases} g_\chi f_\chi^{\rm FI,\,dec}(q_\star) = 2g_B\dfrac{R_\Gamma^{\rm FI}}{\delta^3}\sqrt{\pi} \times \left[\dfrac{1}{q_\star^{1/2}}\exp(-q_\star)\right] & \text{for FI through decays,} \\ g_\chi f_\chi^{\rm SW}(q_\star) = \dfrac{4\sqrt{\pi R_\Gamma^{\rm SW}}C_{\rm SW}}{\delta^2} \times \left[\dfrac{1}{q_\star}\exp\left(-q_\star^2\right)\right] & \text{for SW,} \end{cases} \tag{2.31}$$

where the superscript FI or SW in R_Γ reminds that the number of relativistic dof in M_0 have to be determined at $T_{\rm FI}$ or $T_{\rm SW}$. The resulting dimensionless variables `T_ncdm` which are provided as an input to the CLASS code then read

$$\begin{cases} \texttt{T\_ncdm}^{\rm FI} = \delta \times \left(\dfrac{g_{*S}(t_0)}{g_{*S}(T_{\rm FI})}\right)^{1/3} & \text{and } T_{\rm FI} = \frac{1}{3}m_B, \\ \texttt{T\_ncdm}^{\rm SW} = \dfrac{\delta}{\sqrt{2R_\Gamma^{\rm SW}}} \times \left(\dfrac{g_{*S}(t_0)}{g_{*S}(T_{\rm SW})}\right)^{1/3} & \text{and } T_{\rm SW} = \sqrt{\frac{R_\Gamma}{2}}m_B. \end{cases} \tag{2.32}$$

JCAP03(2022)041

Notice that the momentum dependence of the SW distribution in eq. (2.31) is the same as in the case of moduli decay in a radiation dominated era, considered in [31]. Let us also mention that in the case of FI through scatterings and under the same assumptions used to derive eq. (2.25), we expect a similar $q_\star$ dependence as in the case of FI through decays, but the prefactor would become cross-section dependent instead of decay-rate dependent, see section 2.3 for details. Finally, using the above parametrisation in eq. (2.9), the mean rescaled momenta $\langle q_\star \rangle$ and the mean rescaled squared momenta $\langle q_\star^2 \rangle$ reduce to

$$\begin{cases} \langle q_\star \rangle_{\rm FI,\,dec} = \dfrac{5}{2}, \quad \langle q_\star^2 \rangle_{\rm FI,\,dec} = \dfrac{35}{4} & \text{for FI through decays,} \\ \langle q_\star \rangle_{\rm SW} = \dfrac{\sqrt{\pi}}{2}, \quad \langle q_\star^2 \rangle = 1 & \text{for SW.} \end{cases} \tag{2.33}$$

Following the discussion in section 2.3, we can just replace the equality sign with $\lesssim$ in the case of FI through scatterings.

We will now use the different quantities introduced in this subsection in order to characterise the typical NCDM cosmological imprint of FIMP DM and the associated constraints in the next section.

3 Imprint of FIMPs on cosmological observables

Once FIMPs have been produced at a time where the standard model bath temperature is $T = T_{\rm prod}$, with $T_{\rm prod} = T_{\rm FI}$ ($T_{\rm SW}$) for production from the FI (SW) mechanism, the resulting DM particles free-stream. If their velocity is sufficiently large at late times, they can free-stream from overdense to underdense regions and prevent small-scale structure formation. Furthermore, if FIMPs are still relativistic at Big Bang Nucleosynthesis (BBN) or Cosmic Microwave Background (CMB) times, they constitute extra radiation dof that might be constrained by $\Delta N_{\rm eff}$ bounds.

In sections 3.1 and 3.2 we study the resulting constraints on cosmological observables. We show that when the DM abundance $\Omega_\chi h^2 = 0.12$ results at 100 % from the FI or from the SW mechanism, Lyman-α data provide a lower bound on the DM mass of the form

$$m_\chi \gtrsim \begin{cases} m_{\rm FI}^{\rm lim} \times \delta \times \left(\dfrac{106.75}{g_{*S}(T_{\rm FI})} \right)^{1/3} & \text{for FI through decays,} \\ m_{\rm SW}^{\rm lim} \times \delta \times \left(\dfrac{106.75}{g_{*S}(T_{\rm SW})} \right)^{1/3} \times \left(R_\Gamma^{\rm SW} \right)^{-1/2} & \text{for SW,} \end{cases} \tag{3.1}$$

where the prefactors $m_{\rm FI,SW}^{\rm lim}$ are in the keV mass range, see the summary in table 1. The results for FI are valid for FI from decays as well as for any FI from scattering scenario that would give rise to an equality in eq. (2.27). Our results for FI are in very good agreement with the previous literature in [23, 30–32] when using the same methodology,[7] see also e.g. [40, 41] for similar results obtained in a slightly different context. On the other hand, for mixed FI-SW scenarios a more detailed analysis is needed, see section 3.1.3.

[7] Let us in particular emphasise that for the fit to the power spectrum and the area criterion, our results are obtained by switching the perfect fluid approximation off in CLASS, which is the only valid approximation for generic NCDM, see the discussion in appendix C.

JCAP03(2022)041

Probe	NCDM test	$m_{\rm FI}^{\rm lim}$ [keV]	$m_{\rm SW}^{\rm lim}$ [keV]
Lyman-α	Velocity dispersion, section 3.1.1	16	3.8
	Fits to transfer function, see section 3.1.2	15	3.9
	Area criterion, see section 3.1.3	15	3.8
$\Delta N_{\rm eff}$	see section 3.2	1.3×10^{-2}	3.4×10^{-3}

Table 1. Mass scales in keV entering into the lower bounds of the FIMP masses of eq. (3.1). They arise from the FIMP NCDM imprint on cosmological structures assuming that 100% of the DM content results from FI or SW mechanism production. The values for $m_{\rm FI,SW}^{\rm lim}$ correspond to the WDM bounds $m_{\rm WDM}^{\rm Ly\alpha} > 5.3$ keV and $\Delta N_{\rm eff}(T_{\rm BBN}) < 0.31$.

3.1 FIMP free-streaming and Lyman-α bound

The Lyman-α forest flux power spectrum probes hydrogen clouds at redshifts $2 \lesssim z \lesssim 6$. It provides constraints on the matter power spectrum on small scales [10, 42]. The scales tested by Lyman-α data, typically 0.5 Mpc/h $< \lambda <$ 100 Mpc/h [25], are in the non-linear regime so that computationally expensive hydrodynamical N-body simulations would be required in order to properly test a given NCDM scenario. These expensive simulations have been performed for thermal WDM. Following the early work of [6], the analysis of [7] obtained a bound of $m_{\rm WDM}^{\rm Ly\alpha} = 5.3\,$keV at 95 % confidence level (CL) from Lyman-α flux observations. It has, however, been argued that the assumptions made about the instantaneous temperature and pressure effects of the intergalactic medium in this work might have been too strong. Relaxing these assumptions [8] found a bound of $m_{\rm WDM}^{\rm Ly\alpha} = 1.9\,$keV at 95 % CL. We take the latter as a conservative bound on the thermal WDM mass while the one of [7] will be considered as a stringent bound.

To circumvent the need for new N-body simulations for these models, in this paper we implement the FIMP distribution functions discussed in section 2.4 in the Boltzmann code CLASS. We use this to extract the linear matter power spectrum of our NCDM scenarios, as well as the corresponding transfer functions discussed in section 3.1.2. We then follow a strategy similar to those applied to NCDM in e.g. [23, 25, 31, 32, 37]. In sections 3.1.1 and 3.1.2 we extract a lower bound on the DM mass in pure FI and SW scenarios, making use of the DM velocity dispersion and of fits to the transfer functions. Notice that these constraints are only valid for FIMPs accounting for 100% of the DM content. In section 3.1.3, we address the case of the mixed FI-SW scenarios, or equivalently cases where a given production mechanism cannot account for all the DM, by applying the area criterion introduced in [25].

3.1.1 Velocity dispersion

If the DM distribution is simple, e.g. with one local maximum, one can expect that an estimate of the bound on the FIMP mass can be derived by comparing the typical velocity of the NCDM candidate to the one of the thermal WDM for which dedicated hydrodynamical simulations have been performed. Here we follow the same approach as the one proposed by [23], where an estimated Lyman-α bound was obtained by considering the root mean square (rms) velocity of DM today, $\sqrt{\langle p^2 \rangle_0}/m_\chi$. Here $\langle p^2 \rangle_0$ refers to today's second moment of the momentum distribution, directly related to the velocity dispersion of the DM today. When DM arises from one single production mechanism or production channel $\sqrt{\langle p^2 \rangle_0}/m_\chi =$

$\sqrt{\langle q_\star^2\rangle}\mathtt{T}_{\mathtt{ncdm}}/m_\chi T_\gamma(t_0)$. The lower bound

$$m_\chi \gtrsim 1.75\,\mathrm{keV} \times \sqrt{\langle q_\star^2\rangle}\mathtt{T}_{\mathtt{ncdm}} \times \left(\frac{m_{\rm WDM}^{\rm Ly\alpha}}{\rm keV}\right)^{4/3} \tag{3.2}$$

is obtained imposing that the rms velocity, $\sqrt{\langle p^2\rangle_0}/m_\chi$, computed for a FIMP of mass m_χ equals the rms velocity for a thermal WDM candidate of mass $m_{\rm WDM}^{\rm Ly\alpha}$ saturating the Lyman-α bound. Notice that $\sqrt{\langle q_\star^2\rangle}$ in eq. (3.2) corresponds to the warmness parameter $\tilde{\sigma}$ of [23] and that [31] derived the same constraints by equating the equation of states of the FIMP and the WDM following the early work of [43]. Eq. (3.2) was also used in [32] in the context of FI to be compared to other methodologies. In those references it has already been argued that eq. (3.2) can provide a very good estimate of the Lyman-α constraint for FIMPs. Additionally, in [44] the DM velocity is computed in order to derive constraints on the WDM arising from the SW mechanism, and perfectly agrees with the rms velocity used here to extract Lyman-α constraints. Using the stringent WDM limit $m_{\rm WDM}^{\rm Ly\alpha} = 5.3\,\mathrm{keV}$ from [7], the Lyman-α bound on FIMP DM of eq. (3.2) gives the lower bound on the DM mass reported in eq. (3.1) with $m_{\rm FI}^{\rm lim} = 16\,\mathrm{keV}$ and $m_{\rm SW}^{\rm lim} = 3.8\,\mathrm{keV}$, as given in the first line of table 1. When using the conservative bound of $m_{\rm WDM}^{\rm Ly\alpha} = 1.9\,\mathrm{keV}$ from [8] the prefactors in eq. (3.1) reduce to $m_{\rm FI}^{\rm lim} = 4.0\,\mathrm{keV}$ and $m_{\rm SW}^{\rm lim} = 0.97\,\mathrm{keV}$.

In the cases where NCDM would only account for part of the DM content a dedicated analysis should be performed to compare to the case of thermal WDM [45]. However, as suggested in [23], when multiple production channels are at the origin of the DM relic abundance but the total DM distribution is unimodal, one can still use the rms velocity $\sqrt{\langle p^2\rangle_0}/m_\chi$ to extract a bound on the DM mass. Considering the definition of the second moment of the momentum distribution, it can be shown that

$$\frac{\sqrt{\langle p^2\rangle_0}}{m_\chi} = \frac{T_\gamma(t_0)}{m_\chi}\left(\sum_{\rm prod}\left(\frac{\Omega_\chi h^2|_{\rm prod}}{\Omega_\chi h^2}\right) \times \left(\langle q_\star^2\rangle \mathtt{T}_{\mathtt{ncdm}}^2\right)|_{\rm prod}\right)^{1/2}, \tag{3.3}$$

where the sum runs over the FIMP production mechanisms, $\Omega_\chi h^2|_{\rm prod}$ refers to the χ relic abundance from a given production channel while $\Omega_\chi h^2$ refers to the total relic abundance. A first naive estimate of the Lyman-α bound in the case of mixed scenarios could thus be extracted by comparing the quantity $\sqrt{\langle p^2\rangle_0}/m_\chi$ to the one of thermal WDM saturating the Lyman-α bound when $\Omega_\chi h^2 = 0.12$. Within this framework, we get

$$m_\chi \gtrsim 1.75\,\mathrm{keV} \times \left(\frac{m_{\rm WDM}^{\rm Ly\alpha}}{\rm keV}\right)^{4/3} \times \left[\sum_{\rm prod}\left(\frac{\Omega_\chi h^2|_{\rm prod}}{0.12}\right) \times \left(\langle q_\star^2\rangle \mathtt{T}_{\mathtt{ncdm}}^2\right)|_{\rm prod}\right]^{1/2}, \tag{3.4}$$

where it has been assumed that $\Omega_\chi h^2 = 0.12$ in order to compare to the thermal WDM constraints. Let us emphasise that eq. (3.4) is only valid if the total FIMP distribution, arising from different production processes, is unimodal. This is, for example, the case of FIMPs from FI through scatterings and decays analysed in e.g. [23]. When the DM distribution is multimodal, as e.g. in a mixed FI-SW scenario, the area criterion introduced in [25] should be used instead, see the discussion in section 3.1.3 below.

JCAP03(2022)041

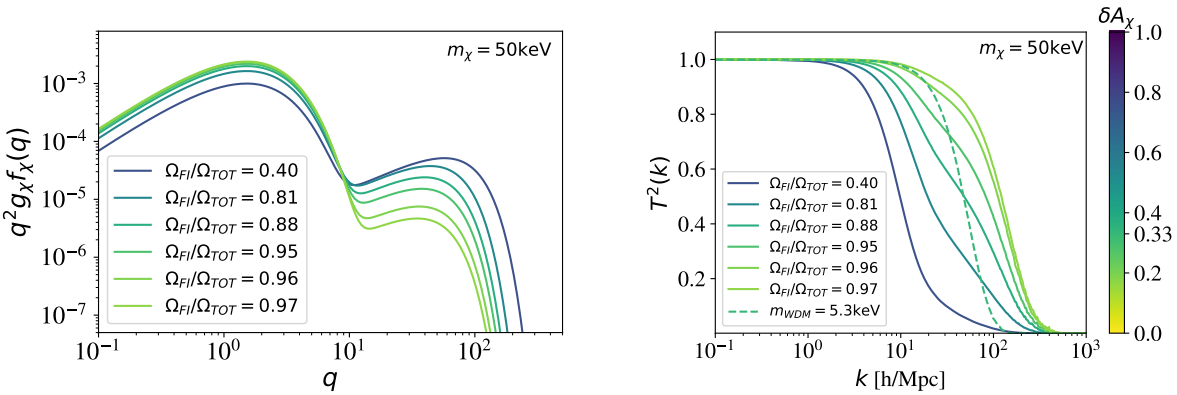

Figure 2. *Left:* distribution functions, $q^2 g_\chi f_\chi(q)$, as a function of the rescaled momentum q for an example FIMP model. *Right:* corresponding transfer functions (continuous coloured curves) as a function of the wavenumber k. The thermal WDM transfer function for $m_{\rm WDM}^{\rm Ly\alpha} = 5.3$ keV (dashed curve) is also shown for comparison. These curves are obtained assuming the DM model considered in section 4 and choosing the DM mass to be 50 keV. Fixing $\Omega_\chi h^2 = 0.12$, the remaining model parameters were varied such that the relative FI contribution ranges from 40% to 97%, see section 4 for details. Going from purple to green indicates going from warmer to colder DM or equivalently going to a smaller value of the area criterion parameter δA_χ, see section 3.1.3 for details.

3.1.2 Fits to transfer function

In order to parametrise the small-scale suppression of the matter power spectrum within a given NCDM model with respect to the equivalent CDM case, one can express the ratio between the CDM power spectrum, $P_{\rm CDM}(k)$, and the power spectrum of some new DM species X, $P_X(k)$, in terms of the transfer function T_X, defined as

$$P_X(k) = P_{\rm CDM}(k)\, T_X^2(k)\,, \tag{3.5}$$

where k is the wavenumber. It has been shown that the transfer function for some NCDM scenarios can be parametrised in terms of a finite set of parameters and physical inputs.

In particular, in the thermal WDM case, [5, 24] use the following parametrisation to describe the transfer function,

$$T_X(k) = \left(1 + (\alpha_X k)^{2\mu}\right)^{-5/\mu}\,, \tag{3.6}$$

where μ is a dimensionless exponent and α_X is the breaking scale. A more general parametrisation that can be applied to a larger set of NCDM models was also introduced in [25, 46, 47].

In the case of thermal WDM, [5] obtained a very good fit for α and μ from dedicated N-body simulations. We will make use of this fit, but with a minor modification to the numerical prefactor motivated in appendix C, where we also discuss the validity of this prescription. As such, the breaking scale we will use for eq. (3.6) is given by $\mu = 1.12$ and

$$\alpha_{\rm WDM} = 0.045 \left(\frac{m_{\rm WDM}}{1\,{\rm keV}}\right)^{-1.11} \left(\frac{\Omega_{\rm WDM}}{0.25}\right)^{0.11} \left(\frac{h}{0.7}\right)^{1.22} h^{-1}{\rm Mpc}\,, \tag{3.7}$$

in terms of the WDM mass $m_{\rm WDM}$.

In the case of FIMPs from the FI and SW production mechanisms, the transfer function can take multiple forms. In the right panel of figure 2, we illustrate the transfer functions

JCAP03(2022)041

computed with CLASS from the distributions shown in the left panel. They correspond to different benchmark scenarios all giving rise to $\Omega_\chi h^2 = 0.12$ within the top-philic DM model described in section 4. Each benchmark has a different FI relative contribution to the total DM relic abundance ranging from 40% (dark purple) to 97% (light green). This is visible in the left panel as the FI contribution to the DM distribution function, that peaks around $q = 2.5$, increases in amplitude when going from the dark purple to the light green curve. In the right panel, we see that when e.g. the FI contribution tends to 100%, the FIMP transfer function recovers the shape of a thermal WDM transfer function, depicted with a dashed curve for $m_{\rm WDM}^{\rm Ly\alpha} = 5.3\,{\rm keV}$. This has already been pointed out in earlier works, see [30, 31]. Similarly, for 100% SW contribution, the FIMP transfer function resembles a WDM-like shape. For intermediate relative FI or SW contribution though, the shape of the transfer function can strongly deviate from thermal WDM like scenarios.

Using our modified CLASS version, we have checked that the transfer function of eq. (3.6) provides a very good fit to the case of DM produced purely through the FI or SW mechanisms. For the fitting curves using $\mu = 1.12$, as in the thermal WDM case, we obtain

$$\alpha_{\rm FI,\,dec} = 0.164 \left(\frac{m_\chi}{1\,{\rm keV}} \times \frac{1}{\delta}\right)^{-0.833} \left(\frac{g_{*S}(t_0)}{g_{*S}(T_{\rm FI})}\right)^{0.278} h^{-1}{\rm Mpc}\,, \tag{3.8}$$

$$\alpha_{\rm SW} = 0.0542 \left(\frac{m_\chi}{1\,{\rm keV}} \times \frac{\sqrt{R_\Gamma^{\rm SW}}}{\delta}\right)^{-0.833} \left(\frac{g_{*S}(t_0)}{g_{*S}(T_{\rm SW})}\right)^{0.278} h^{-1}{\rm Mpc}\,, \tag{3.9}$$

where the parameter dependency of the breaking scales was inspired by the analytic estimate of the Lyman-α bound of eq. (3.2). The numerical prefactors in eqs. (3.8) and (3.9), on the other hand, have been obtained by doing a one-parameter fit based on the actual transfer functions produced by CLASS. In the case of FI, the fit was done over 15 models, with a final error on the prefactors of $\sim 1.5\%$. In the case of SW, we used 20 models for the fit, with an expected error of $\sim 2\%$. In both cases, the fit has been optimised in the mass range where we expect the Lyman-α constraints to appear, based on eq. (3.1) (see appendix C for further discussions).

In similar spirit to what was done in e.g. [37], we can now compare the breaking scales ($\alpha_{\rm FI}$ and $\alpha_{\rm SW}$) found in eqs. (3.8) and (3.9) with the breaking scale for WDM ($\alpha_{\rm WDM}$) from eq. (3.7), to obtain approximate Lyman-α bounds on FIMP DM. Assuming once more that the DM is produced at 100% through the FI or SW mechanisms and that this accounts for all of the DM abundance, taking the stringent WDM limit $m_{\rm WDM}^{\rm Ly\alpha} = 5.3\,{\rm keV}$ from [7] we get $m_{\rm FI}^{\rm lim} = 15\,{\rm keV}$ and $m_{\rm SW}^{\rm lim} = 3.9\,{\rm keV}$ in eq. (3.1), see the second line of table 1. We can see that these bounds are in very good agreement with the approximate constraints found in section 3.1.1 using the rms velocity. When using the conservative bound of $m_{\rm WDM}^{\rm Ly\alpha} = 1.9\,{\rm keV}$ from [8] these prefactors reduce to $m_{\rm FI}^{\rm lim} = 3.5\,{\rm keV}$ and $m_{\rm SW}^{\rm lim} < 1.0\,{\rm keV}$.

3.1.3 Area criterion

An alternative approach to extract the Lyman-α bounds on NCDM scenarios is based on the area criterion introduced in [25], see also [26, 32, 48]. The methodology goes as follows. For a given DM scenario X, the 3D power spectrum $P_X(k)$ has to be computed. The deviation from the corresponding CDM scenario is obtained by evaluating the ratio

$$r(k) = \frac{P_{\rm 1D}^X(k)}{P_{\rm 1D}^{\rm CDM}(k)} \quad \text{with} \quad P_{\rm 1D}^X(k) = \int_k^\infty {\rm d}k'\, k'\, P_X(k')\,, \tag{3.10}$$

where $P_{\rm 1D}^X$ is the 1D power spectrum in the DM scenario X.

JCAP03(2022)041

This ratio is estimated over the range of scales probed by the Lyman-α observations. In [25] the suggested range corresponding to the MIKE/HIRES+XQ-100 combined data set, used in [11] to derive the stringent WDM bound considered here, was taken to be

$$[k_{\rm min}, k_{\rm max}] = [0.5\,{\rm h/Mpc}, 20\,{\rm h/Mpc}]\,. \tag{3.11}$$

More precisely, in order to quantify the suppression of the power spectrum in the NCDM model X, one should compute the area estimator

$$\delta A_X = \frac{A_{\rm CDM} - A_X}{A_{\rm CDM}} \quad \text{with} \quad A_X = \int_{\rm k_{min}}^{k_{\rm max}} {\rm d}k'\, r(k')\,, \tag{3.12}$$

and $A_{\rm CDM} = k_{\rm max} - k_{\rm min}$ by definition.

As underlined by the authors of the original work [25] introducing this criterion, let us emphasise that the area criterion has some arbitrariness in defining the integration limits, and should, therefore, only be used after careful calibration with an example WDM model. For the cosmological and precision parameters considered in our analysis, we get

$$\delta A_{\rm WDM} = 0.33 \quad \text{for} \quad m_{\rm WDM} = 5.3\,{\rm keV}. \tag{3.13}$$

A NCDM scenario that would give rise to $\delta A_X = \delta A_{\rm WDM}$ above is thus expected to saturate the stringent WDM Lyman-α bound considered here.[8]

Making use of the linear 3D power spectrum computed with our modified version of CLASS for pure FI and SW DM scenarios and, comparing $\delta A_{\rm FI,\,dec}$ and $\delta A_{\rm SW}$ to the stringent bound provided by eq. (3.13), we get a limit similar to the one derived in sections 3.1.1 and 3.1.2. More precisely, for the prefactors of eq. (3.1), we get $m_{\rm FI}^{\rm lim} = 15\,{\rm keV}$[9] and $m_{\rm SW}^{\rm lim} = 3.8\,{\rm keV}$, see the third line of table 1. We have also checked that using the fits provided in eqs. (3.8) and (3.9) instead of the $P(k)$ from CLASS gives rise to the same conclusions. It appears, therefore, that in the case of pure FI or SW, all 3 methodologies considered in section 3.1 agree with each other. In particular, this suggests that a very accurate estimate of the Lyman-α bound, for FIMP scenarios with unimodal distribution functions, can readily be extracted from eq. (3.2) without going through the detailed implementation of the NCDM model in CLASS. In contrast, a more advanced approach proposed in [47], where a Lyman-α likelihood was developed for multiple NCDM models, allows for full Monte Carlo Markov Chain (MCMC) analyses. However, such analyses are hindered by the execution speed of the corresponding NCDM model in CLASS. For the models considered here, the corresponding runtime needed to calculate the matter power spectrum is of the order of $\sim 30\,{\rm min}$ per model,[10] making MCMC analyses computationally infeasible. As such, here we limit ourselves to the more simplistic methods discussed above.

In the case of mixed FI-SW scenarios, the DM distribution function is multimodal and the resulting transfer function can significantly deviate from the WDM one, as illustrated in figure 2. The area criterion is the only estimator of the Lyman-α bound that has been carefully tested against hydrodynamical simulations for a large ensemble of NCDM scenarios,

[8] Notice that in [25], a much smaller $\delta A_{\rm WDM}$ of 0.21 is reported for a 5.3 keV WDM. We have checked together with R. Murgia of [25] that the methodology followed here is perfectly correct. A discrepancy with the numerical results for $\delta A_{\rm WDM}$ quoted in [25] has also been reported in e.g. [32]. This emphasises the importance of recomputing self-consistently the $\delta A_{\rm WDM}$ before applying any constraint to a new NCDM scenario.

[9] Note that if we make use of the perfect fluid approximation in CLASS, we obtain $m_{\rm FI}^{\rm lim} = 16\,{\rm keV}$, as in [32]. However, we will switch this approximation off for NCDM from FI, see appendix C.

[10] See appendix C for more details on the computation time.

JCAP03(2022)041

see [25, 49]. For this reason, we make use of the latter criterion when considering mixed FI-SW models. In particular, for the set of benchmarks of figure 2, the gradient of colours in the curves corresponds to a value of the area criterion. More precisely, going from purple to green curves we have $\delta A_\chi = (0.75, 0.54, 0.38, 0.29, 0.20, 0.18)$, respectively, i.e. the first three benchmarks are excluded when considering eq. (3.13). We have also checked that the area criterion gives rise to a more conservative bound than the estimator of eq. (3.4) for mixed scenarios. As a result, for mixed FI-SW scenarios, it necessary to implement the exact NCDM model in CLASS in order to extract a reliable estimate of the Lyman-α bound.

3.2 Bound from $\Delta N_{\rm eff}$

The FIMPs considered here can potentially affect the effective number of relativistic non-photonic species, $N_{\rm eff}$, entering in the computation of CMB and BBN observables, see e.g. [31, 38, 39]. Here we consider the possibility for the DM candidates to contribute as an extra fermionic species. Our goal is, therefore, to compute their $\Delta N_{\rm eff}(T)$ contribution at a given temperature T, corresponding to a given scale factor $a(T)$. It is instructive to first estimate for which mass range FIMPs arising from FI or SW are still relativistic. This is the case when the rescaled momentum $\langle q_\star \rangle$ is larger than the ratio $m_\chi/T_\star$. Using eqs. (2.32) and (2.33), the condition on the FIMP mass becomes

$$m_\chi > \begin{cases} \dfrac{\delta}{a\,(T)} \times 2 \times 10^{-7}\,\text{keV} & \text{for relativistic FIMP from FI,} \\ \dfrac{\delta}{a\,(T)\,R_\Gamma^{1/2}} \times 5 \times 10^{-8}\,\text{keV} & \text{for relativistic FIMP from SW,} \end{cases} \tag{3.14}$$

when $g_{*S}\,(T_{\rm prod}) = 106.75$. From section 3.1, we know that for FIMPs from FI, Lyman-α forest data imply a lower bound on their mass of around 15 keV. FIMPs from FI with larger masses cannot be further constrained by $\Delta N_{\rm eff}$ bounds from CMB data, as they are expected to be highly non-relativistic for $a(T_{\rm CMB}) \sim 10^3$. For FIMPs from SW, with mass $m_\chi > 10\,\text{keV}$ we would need $R_\Gamma > 10^{-14}$ for them to be non-relativistic at CMB time. On the other hand, since $a\,(T_{\rm BBN}) \sim 10^{-10}$, one can more easily get relativistic FIMPs from both FI and SW at BBN time. We will, therefore, focus on $\Delta N_{\rm eff}$ at BBN time and impose the bound [50]

$$\Delta N_{\rm eff}(T_{\rm BBN}) < 0.31\,, \tag{3.15}$$

at 95% CL, see also [51, 52].

We compute the FIMP contribution to the effective number of relativistic non-photonic species, $\Delta N_{\rm eff}\,(T)$, following [38]. In general, at a given bath temperature T, we should evaluate

$$\begin{aligned} \Delta N_{\rm eff}(T) &= \frac{\rho_\chi(T) - m_\chi n_\chi(T)}{\rho_{{\rm rel}\,\nu}(T)/N_{\rm eff}^\nu} \\ &= g_\chi \frac{60}{7\pi^4} \left(\frac{T_\star}{T_\nu}\right)^4 \times \int {\rm d}q_\star q_\star^2 \left(\left(q_\star^2 + \frac{m_\chi^2}{T_\star^2} \right)^{1/2} - \frac{m_\chi}{T_\star} \right) f(q_\star)\,, \end{aligned} \tag{3.16}$$

where $\rho_{{\rm rel}\,\nu}/N_{\rm eff}^\nu = 2 \times \frac{7}{8}\frac{\pi^2}{30} T_\nu(T)^4$ is the energy density per relativistic standard model neutrino and $T_\star, T_\nu$ are time-dependent variables. For relativistic FIMPs at BBN time, this contribution reduces to

$$\Delta N_{\rm eff}^{\rm rel}\,(T_{\rm BBN}) \simeq \left.\frac{\rho_\chi^{\rm rel}}{\rho_{{\rm rel}\,\nu}/N_{\rm eff}^\nu}\right|_{T_{\rm BBN}} = \langle q_\star \rangle \times \left.\frac{T_\star n_\chi}{\rho_{{\rm rel}\,\nu}/N_{\rm eff}^\nu}\right|_{T_{\rm BBN}}\,. \tag{3.17}$$

JCAP03(2022)041

Rescaling $T_\star n_\chi$ from BBN time to today, keeping in mind that $\langle q_\star \rangle$ is constant, and that $T_\nu(T) = T$ at BBN time, we get

$$\Delta N_{\rm eff}^{\rm rel}(T_{\rm BBN}) \simeq 5.0 \times 10^{-4} \times \langle q_\star \rangle_{\mathtt{T_{ncdm}}} \times \left(\frac{\Omega_\chi h^2}{0.12}\right)\left(\frac{10\,\text{keV}}{m_\chi}\right), \tag{3.18}$$

where $\Omega_\chi h^2$ is the non-relativistic FIMP abundance today. Using the values of $\langle q_\star \rangle_{\mathtt{T_{ncdm}}}$ obtained above and the condition eq. (3.15) we find

$$m_\chi \gtrsim \begin{cases} 1.3 \times 10^{-2}\,\text{keV} \times \delta \left(\dfrac{\Omega_\chi^{\rm FI} h^2}{0.12}\right)\left(\dfrac{106.75}{g_{*S}(T_{\rm FI})}\right)^{1/3} & \text{for FI}, \\ 3.4 \times 10^{-3}\,\text{keV} \times \delta \left(R_\Gamma^{\rm SW}\right)^{-1/2}\left(\dfrac{\Omega_\chi^{\rm SW} h^2}{0.12}\right)\left(\dfrac{106.75}{g_{*S}(T_{\rm SW})}\right)^{1/3} & \text{for SW}, \end{cases} \tag{3.19}$$

where $\Omega_\chi^{\rm FI,SW}$ refers to the FIMP abundance arising from FI or SW production.[11] At first sight, the above constraints seem less constraining than Lyman-α, in agreement with [31], see also [53]. Notice, however, that contrarily to e.g. eq. (3.1), the above constraints are applicable even when $\Omega_\chi h^2 < 0.12$.[12]

4 FIMPs within a top-philic mediator model

For an application of the above results and their comparison to other constraints we consider a simplified t-channel mediator DM model. It supplements the standard model with a singlet Majorana fermion, χ, and a coloured scalar mediator, $\tilde{t}$, with gauge quantum numbers identical to the right-handed top quark. Imposing a Z_2 symmetry under which $\chi \to -\chi$ and $\tilde{t} \to -\tilde{t}$ (while standard model particles transform evenly), χ is stable for $m_\chi < m_{\tilde{t}}$ and, hence, constitutes a viable DM candidate. The renormalisable interactions allowed by the Z_2 and gauge symmetries are described by the Lagrangian

$$\mathcal{L}_{\rm int} = |D_\mu \tilde{t}|^2 + \lambda_\chi \tilde{t}\,\bar{t}\,\frac{1-\gamma_5}{2}\chi + \text{h.c.} + \lambda_{H\tilde{t}}\,\tilde{t}^\dagger \tilde{t} H^\dagger H\,, \tag{4.1}$$

where D_μ is the covariant derivative, t the top quark Dirac field and H the standard model Higgs doublet. The masses $m_\chi, m_{\tilde{t}}$ and the coupling λ_χ are the phenomenologically relevant parameters considered here. The latter governs the (feeble) DM interactions with the thermal bath. The Higgs portal coupling, $\lambda_{H\tilde{t}}$, affects the interactions of the mediator with the thermal bath. For DM production via FI, during which the mediator is in thermal equilibrium, the presence of this coupling does not affect the relevant dynamics. For the case of SW production, it can contribute to the mediator annihilation during its freeze-out, potentially lowering its abundance. However, to compete with the annihilation rate associated with the strong interactions of the mediator (which are further enhanced through non-perturbative effects, see below) requires the Higgs portal coupling to be very large. Here we assume $\lambda_{H\tilde{t}}$ to be well below unity, in which case it is totally negligible for the phenomenology considered.

[11] The FI constraint in eq. (3.19) can be applied to FI through scatterings by setting $\delta = 1$ when the conditions to extract eq. (2.33) are met.

[12] Also notice that our results for SW do not agree with the results of [39]. Let us re-emphasise, however, that [39] assumed that B is kinetically decoupled after FO, which is usually not the case if B is charged under standard model symmetries.

JCAP03(2022)041

The model is reminiscent of a supersymmetric standard model. In fact, it may be realised as a limiting case of a non-minimal supersymmetric extension in which χ is a mixture of the bino and the fermionic component of an additional supermultiplet that is a singlet under the standard model gauge group [54, 55]. However, we will remain agnostic to a possible theoretical embedding of the simplified model, assuming that the above Lagrangian captures the relevant physics.

In the context of FI and SW production, this model has been studied in [27]. Similar results have been obtained for other spin-assignments [56, 57]. A variant of the model without an imposed Z_2 symmetry was discussed in [58, 59], while its phenomenology in the case of thermalised DM can be found in [60, 61].

In [27], constraints from Lyman-α forest observations have been estimated with a comparison of the respective limits on the free-streaming length obtained for WDM from [45]. Here we revisit the phenomenology and improve the analysis with respect to [27] in two main aspects. First, we improve the structure formation bounds utilising the methodology outlined in sections 2 and 3. In particular, computing the DM phase-space distribution and making use of the area criterion, we can derive a reliable and more stringent bound in the region of mixed FI and SW production. Second, we take into account bound state formation effects in the mediator freeze-out, which are relevant for the SW production of DM.

In the following we will first discuss the mediator freeze-out in section 4.1. We will then detail the FI and SW production processes of DM within the model in section 4.2, before deriving the constraints on the model parameter space in section 4.3.

4.1 Mediator freeze-out

For parameter regions with a sizeable SW contribution to the DM production, the DM density (and, in general, its phase-space distribution) depends on the evolution of the mediator abundance governed by thermal freeze-out. This process is subject to non-perturbative effects. On the one hand, gluon exchange between the initial state mediators modifies their wave function, leading to an enhancement with respect to the tree-level annihilation rate at small relative velocities, i.e. the Sommerfeld enhancement [62–64]. On the other hand, mediator pairs can form bound states that affect the freeze-out dynamics leading to a further reduction of the mediator abundance, see e.g. [28, 65–67].

Here we consider both effects in the non-relativistic limit using the computations derived in [28]. Accordingly, for mediator pair-annihilation into gluons, we employ the s-wave annihilation Sommerfeld factor for a Coulomb potential. Mediator pair annihilation into quark pairs is p-wave suppressed and, hence, sub-dominant for small relative velocities. We take into account bound state formation (ionization) via one-gluon emission (absorption) and the leading bound state decay process into a pair of gluons. We consider the ground state configuration only. Furthermore, it is assumed that the rate of bound state number changing processes (formation, ionization or decay) is large compared to all other rates involved in the mediator freeze-out. In this case, the effects of bound state formation can be described by an effective annihilation cross-section [66]. It reads

$$\langle \sigma_{\tilde{t}\tilde{t}^\dagger} v \rangle_{\text{eff}} = \langle \sigma_{\tilde{t}\tilde{t}^\dagger \to gg} v \rangle \times S_{\text{Som}} + \langle \sigma_{\tilde{t}\tilde{t}^\dagger \to q\bar{q}} v \rangle + \langle \sigma_{\tilde{t}\tilde{t}^\dagger \to \mathcal{B}g} v \rangle \times \frac{\Gamma_{\mathcal{B},\text{dec}}}{\Gamma_{\mathcal{B},\text{ion}} + \Gamma_{\mathcal{B},\text{dec}}} \tag{4.2}$$

where S_{Som} is the Sommerfeld enhancement factor, $\langle \sigma_{\tilde{t}\tilde{t}^\dagger \to \mathcal{B}g} v \rangle$ is the thermally averaged bound state formation cross-section, $\Gamma_{\mathcal{B},\text{ion}}$ is the respective ionization rate, $\mathcal{B}g \to \tilde{t}\tilde{t}^\dagger$, and

JCAP03(2022)041

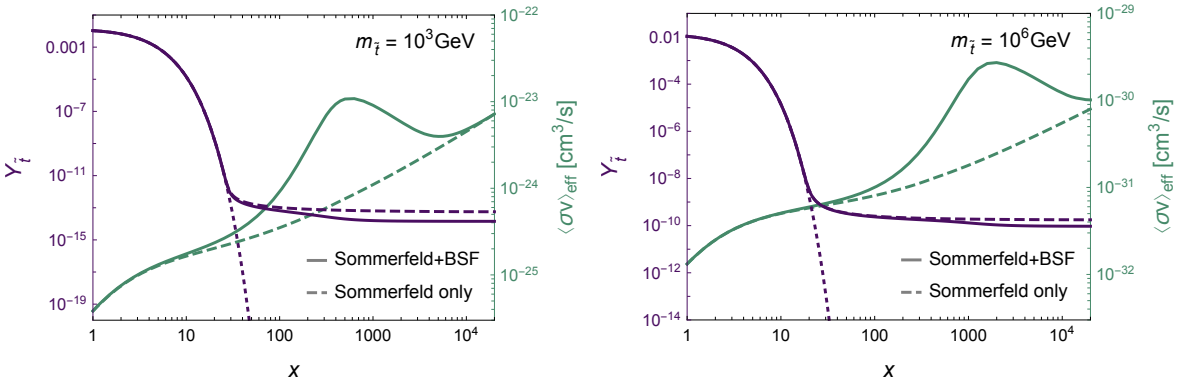

Figure 3. Evolution of the mediator abundance $Y_{\tilde{t}}$ (purple curves, left axes) and the effective annihilation cross-section $\langle\sigma_{\tilde{t}\tilde{t}^\dagger} v\rangle_{\rm eff}$ (green curves, right axes) as a function of $x = m_{\tilde{t}}/T$ for $m_{\tilde{t}} = 10^3$ GeV (left panel) and $m_{\tilde{t}} = 10^6$ GeV (right panel). The solid curves take into account Sommerfeld enhancement and bound state formation effects ('Sommerfeld+BSF') while for the dashed curves only the former has been considered ('Sommerfeld only'). The purple dotted curves denote the mediator equilibrium abundance $Y_{\tilde{t}}^{\rm eq}$.

$\Gamma_{\mathcal{B},\rm dec}$ its decay rate, $\mathcal{B} \to gg$. For further details see appendix B. We compute the thermally averaged annihilation cross-sections for the perturbative processes $\tilde{t}\tilde{t}^\dagger \to gg, q\bar{q}$ with MadDM [68].

Assuming the maintenance of kinetic equilibrium via elastic gluon scattering, $\tilde{t}g \to \tilde{t}g$, throughout the entire freeze-out process, we compute the mediator abundance by solving the integrated Boltzmann equation[13]

$$\frac{\mathrm{d}Y_{\tilde{t}}}{\mathrm{d}x} = \frac{1}{3H}\frac{\mathrm{d}s}{\mathrm{d}x}\left[\frac{1}{2}\langle\sigma_{\tilde{t}\tilde{t}^\dagger} v\rangle_{\rm eff}\left(Y_{\tilde{t}}^2 - Y_{\tilde{t}}^{\rm eq\,2}\right) + \frac{\Gamma_{\tilde{t}}}{s}Y_{\tilde{t}}\right], \tag{4.3}$$

where $Y_{\tilde{t}}$ denotes the summed abundance of the mediator and its antiparticle and $\Gamma_{\tilde{t}}$ is the (thermally averaged) rate for the mediator decay, i.e. for $\tilde{t} \to t\chi$. Figure 3 shows the effective annihilation cross-section and the resulting evolution of $Y_{\tilde{t}}$ for two example mediator masses including Sommerfeld enhancement only (dashed curves) and including bound state effects in addition (solid curves). In these plots, we choose $\Gamma_{\tilde{t}}$ small such that the decay is inefficient in the displayed x-range. The presence of bound states leads to a prolonged freeze-out process, as bound state effects cause an enhancement of $\langle\sigma_{\tilde{t}\tilde{t}^\dagger} v\rangle_{\rm eff}$ at large x. Towards larger mediator masses, the maximum of this enhancement is shifted to higher x, while the effect on the mediator abundance becomes smaller. For a mass 10^3 (10^6) GeV, bound state effects reduce the abundance by a factor of 3.9 (1.9).

4.2 Dark matter production processes

The leading processes to DM production are scatterings of the form $X\tilde{t} \to X'\chi$, where X, X' denote standard model particles, and mediator decays $\tilde{t} \to t\chi$. The latter gives rise to both a FI and SW contribution. The respective vacuum decay rate reads

$$\Gamma_{\tilde{t}\to t\chi} = \frac{\lambda_\chi^2}{16\pi m_{\tilde{t}}^3}\left(m_{\tilde{t}}^2 - m_\chi^2 - m_t^2\right)\lambda^{1/2}\left(m_{\tilde{t}}^2, m_\chi^2, m_t^2\right), \tag{4.4}$$

[13] When the annihilations become inefficient, only the second term in the squared parenthesis of eq. (4.3) is left and we recover eq. (2.16) taken into account for the SW mechanism with $B = \tilde{t}$ in the $x > 1$ limit.

JCAP03(2022)041

where $\lambda(x,y,z) = x^2 + y^2 + z^2 - 2(xy + xz + yz)$. Pair production of DM of the form $XX' \to \chi\chi$ is of higher order in the coupling λ_χ and, hence, neglected here.

Among the scattering processes, we consider the leading processes in the strong coupling α_s, i.e. $t\tilde{t} \to g\chi$ and $g\tilde{t} \to t\chi$, which are expected to contribute similarly. However, the second process is subject to a soft divergence, which we regularise by introducing a thermal mass for the gluon [69];

$$m_g(T) = \frac{4\pi\alpha_s}{6} T^2 \left(N_c + \frac{N_f}{2} + \frac{N_s}{2} \right) , \tag{4.5}$$

where T is the bath temperature, and N_c, N_f, N_s are the number of colours and number of active fermions and scalars in the thermal bath, respectively. The thermal mass enters the cross-section and the lower integration limit, $\tilde{s}_{\min}$, in eq. (2.23). Note that the process belongs to the $\mathcal{O}(\alpha_s)$ corrections to the mediator decay at finite temperatures. Their rigorous computation can only be performed in thermal field theory, which is beyond the scope of this work.[14] Conservatively, we consider the size of the FI contribution from scattering as a rough estimate for the uncertainty of the total FI contribution to the relic density. The scattering processes contribute between 15 and 25% for a mediator mass in the range of 10^3 GeV to 10^{10} GeV. Note that the thermal mass of the gluon introduces a temperature dependence in the cross-section, as well as in the minimal centre of mass energy. As a result, eqs. (2.25) and (2.27) do not apply and the mean momentum shifts to a higher value $\langle q \rangle \approx 3.15$. However, this effect in the total distribution is marginal because the channel $g\tilde{t} \to t\chi$ is suppressed compared to the others when considering the gluon thermal mass as a regulator. This is illustrated in figure 4 for a parameter point with $\lambda_\chi = 10^{-7}$, $m_{\tilde{t}} = 5.6 \times 10^6$ GeV, and $m_\chi = 10^{-3}$ GeV. The total FI distribution is shown with a solid curve, while the contributions from the two scattering processes and the decay are shown with dot-dot-dashed, dotted and dashed curves, respectively.

For very small DM masses, the coupling λ_χ that yields the measured relic density can become large enough to render the decay efficient already close to the time of mediator freeze-out.[15] In this case, the distinction between the FI and SW production processes may be less obvious. For definiteness, we consider the contribution in the regime $x < 7$ ($x > 7$) to belong to the FI (SW) production. We only consider scatterings in the former while taking into account the full evolution of the mediator abundance, solving eq. (4.3), only in the latter regime. This value of x has been chosen since scatterings are already completely negligible at this point. In addition, deviations from thermal equilibrium are still small even for the largest mediator masses considered here, which feature the earliest deviations from thermal equilibrium. Note that the SW contribution from early decays is only comparable to the FI contribution for very large mediator masses, where the larger mediator freeze-out abundance overcompensates the small ratio of masses $m_\chi/m_{\tilde{t}}$ entering the SW contribution to the DM relic density.

4.3 Viable parameter space and constraints

By numerically solving

$$\Omega_\chi h^2|_{\rm FI}(\lambda_\chi) + \Omega_\chi h^2|_{\rm SW}(\lambda_\chi) = 0.12 \tag{4.6}$$

we compute the required DM coupling, λ_χ, that matches the measured relic density for a given DM and mediator mass in the considered parameter space. The resulting hyperplane

[14] See e.g. [70, 71] for recent advances in the treatment of thermal corrections relevant for FI.

[15] For the DM masses around the Lyman-α constraint, decays and scatterings are, however, at least about two orders of magnitude smaller than the Hubble rate for $x \lesssim 3$, justifying the commonly made approximations in the FI computation.

JCAP03(2022)041

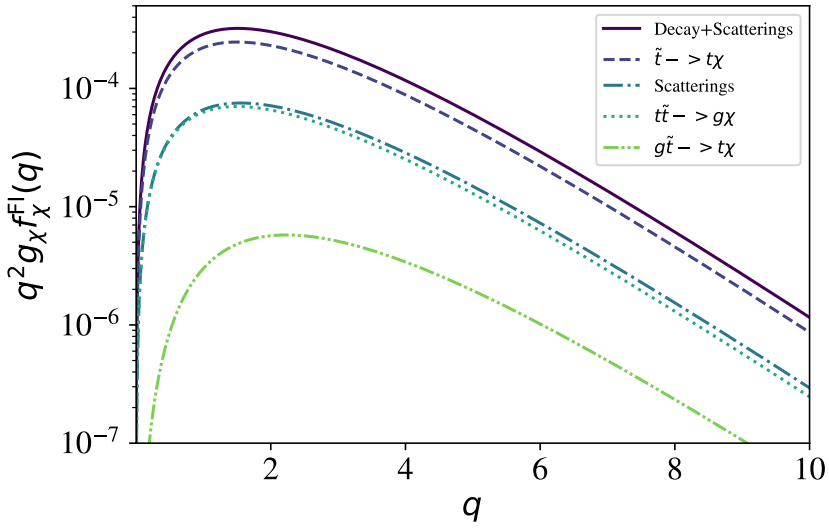

Figure 4. Contributions to the DM distribution function arising from FI, $q^2 g_\chi f_\chi^{\rm FI}(q)$, as a function of q for top-philic DM when taking $\lambda_\chi = 10^{-7}$, $m_{\tilde{t}} = 5.6 \times 10^6$ GeV, and $m_\chi = 10^{-3}$ GeV. From top to bottom we have the total distribution arising from both decays and scattering (solid), as well as the decay (dashed) and the total scattering (dot-dashed) contributions. The latter divides into the $g\tilde{t} \to t\chi$ (dot-dot-dashed) and the $t\tilde{t} \to g\chi$ (dotted) contributions. Because of the gluon thermal mass considered to regularise the scattering cross-section for $g\tilde{t} \to t\chi$, the dot-dot-dashed curve has a mean momentum shifted to higher values than the expected $\langle q \rangle = 2.5$ for FI.

is shown in figure 5 by displaying contours of equal λ_χ in the plane spanned by m_χ and $\Delta m = m_{\tilde{t}} - m_\chi$ (green curves in the left panel) and by drawing contours of equal m_χ in the plane spanned by λ_χ and Δm (cyan curves in the right panel). Note that we have inverted the scale of the abscissa in the right panel to make the correspondence between the two projections more obvious. To the right of the thick black line in the left panel, $\Omega_\chi h^2|_{\rm SW}(\lambda_\chi) > 0.12$ for any λ_χ and so no solution for eq. (4.6) can be found. Approaching this boundary from the left, the coupling drops by orders of magnitude. This region is only visually resolved in the right panel.

The black long-dashed curves denote contours of equal SW contribution. The 50% curve divides the parameter space into the FI (to the left) and SW dominated regions (to the right). In the former the relic density is (asymptotically) proportional to λ_χ^2 while in the latter the λ_χ-dependence is mild. However, due to the prolonged freeze-out process discussed in section 4.1, even the SW contribution depends on λ_χ in a considerable part of the parameter space. In particular, in the region of large mediator masses and significant SW contribution, the mediator decays while mediator pair annihilations have not yet become fully inefficient.

For the computation of the Lyman-α bound on the top-philic DM parameter space, we have exploited the area criterion. As discussed in section 3.1.3, this allows us to probe the mixed FI-SW scenarios encountered in this model. To this aim, we have used our modified version of CLASS including the analytic FI from decay and SW DM distribution functions[16]

[16]Because of the prolonged freeze-out, one should a priori compute the DM distribution arising — from both FI and SW — fully numerically by integrating out the collision term given in eq. (2.21), where f_B would obtained using eq. (2.8) with $Y_B = Y_{\tilde{t}}$ arising from the integrated Boltzmann eq. (4.3). We have checked that using our analytic distributions of section 2.4 with $Y_{\rm FO} = \Omega_\chi h^2|_{\rm SW}(\lambda_\chi) \times \rho_{\rm crit}/(s_0 h^2 m_\chi)$, we recover the numerical results up to a few percent error.

JCAP03(2022)041

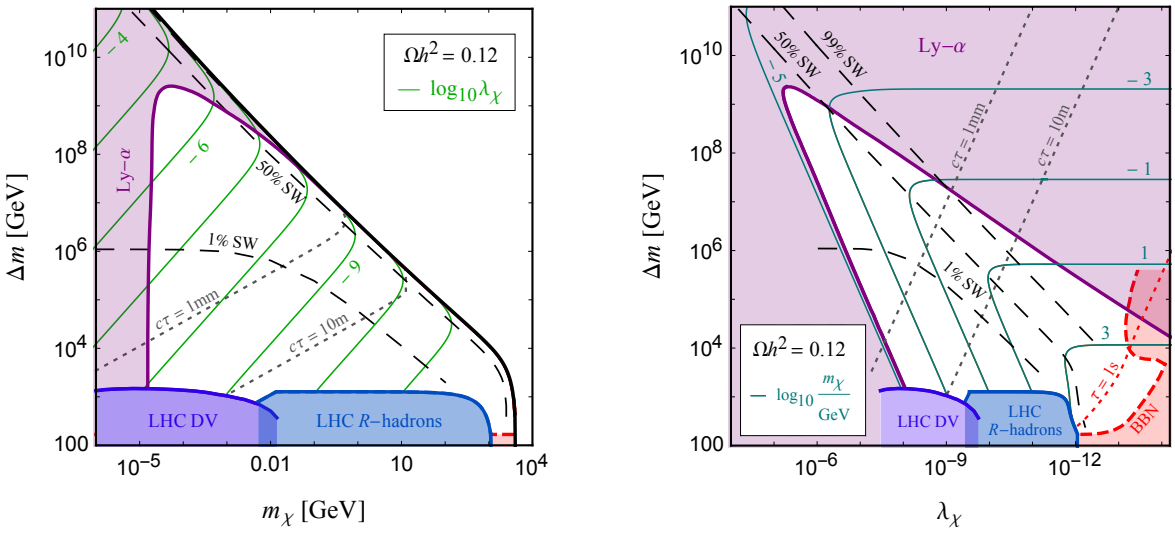

Figure 5. Cosmologically viable parameter space ($\Omega h^2 = 0.12$) of the considered top-philic t-channel mediator model. *Left:* projection onto the plane spanned by m_χ and $\Delta m = m_{\tilde{t}} - m_\chi$. The green contours denote decades of the coupling λ_χ. For parameter points to the right of the thick black line, DM is over-abundant regardless of the coupling, i.e. no solution can be found. *Right:* projection onto the Δm-λ_χ-plane. The cyan contours denote decades of m_χ/GeV. (To reduce clutter we only display every second line.) Note that the scale of the abscissa has been inverted allowing for a more direct comparison of the two projections. In both panels, the black, long-dashed curves denote contours of equal SW contribution to the total relic density. The grey dotted lines denote contours of equal decay length. Our constraints from the Lyman-α observations (Ly-α) are shown in purple, while BBN bounds are displayed in red. Constraints from LHC searches for displaced vertices (DV) and R-hadrons are shown in royal blue and aqua blue, respectively.

displayed in section 2.4, together with fits to the numerically obtained contributions arising from FI via scatterings. We have followed the methodology described in section 3.1.3 for a selection of parameter points which were expected to lie near the Lyman-α limits. An example of this selection is shown in figure 2 for $m_\chi = 50\,\text{keV}$.

The Lyman-α observations constrain the parameter space towards small DM masses (in the FI dominated regime, i.e. to the left), towards small DM couplings and, hence, large mediator lifetimes (in the SW dominated regime, i.e. to the right), and towards large mediator masses (in the mixed regime, i.e. to the top). The exclusion is displayed as the purple shaded region in both panels of figure 5. In the limit of FI and SW dominated production, the limits correspond the ones in eq. (3.1) from the area criterion. Note that the limits are considerably stronger than the ones estimated in [27], in particular, in the region of similar contributions from FI and SW region providing an upper bound on the mediator of around $\Delta m = 2 \times 10^9\,\text{GeV}$.

Towards small mediator masses and towards large mediator lifetimes, the parameter space is constrained by two further observations. First, searches for long-lived coloured particles at the LHC constrain mediator masses up to the TeV scale. Here we illustrate the limits imposed by current data considering searches for R-hadrons and displaced vertices. In the region of parameter space providing large lifetimes compared to the detector size, i.e. for $c\tau > 100\,\text{m}$, we directly apply the limit from the 13 TeV ATLAS search [72] for detector-stable R-hadrons containing a supersymmetric top-partner. For smaller lifetimes, we reinterpret the

JCAP03(2022)041

13 TeV ATLAS search for displaced vertices and missing transverse energy [73] within our model using the recasting from [57]. We use the squark cross-section prediction provided in [74] for the $\tilde{t}$ pair production at the LHC. Second, the decay of the coloured mediator during the epoch of BBN may spoil the successful predictions for the primordial abundances of light elements [75–78]. We estimate these constraints employing the results from [75] for a hadronic branching ratio of 1. The relatively mild dependence of the limits on the mediator mass is approximately taken into account linearly interpolating (and extrapolating) the results for 100 GeV and 1 TeV in log-log space. The same approach was followed in [27].

The LHC and BBN bounds are shown in figure 5 as the blue and red shaded regions, respectively. For small mediator masses, the smaller freeze-out energy density of the mediator required by eq. (4.6) allows for larger lifetimes. In this regime the BBN constraints arise dominantly from the observed primordial abundance of ^{2}H. For larger mediator masses and correspondingly larger energy densities the stronger limits derived from ^{4}He observations dominate, constraining considerably smaller lifetimes. For comparison, we highlight the contour with a lifetime of 1s as the dotted red curve. However, as the derivation of these bounds partly rely on a extrapolation of the results of [75] we consider them as a rough estimate only and leave a dedicated analysis for future work. Noticeable developments of numerical tools for the reinterpretation of BBN bounds have been made more recently, see e.g. [79, 80].

The LHC searches for R-hadrons and displaced vertices exclude mediator masses up to around 1.3 and 1.5 TeV, respectively. Note that the slight gap in their sensitivity for a DM mass between 1 and 10 MeV — corresponding to a mediator decay length of around 10 to 100 m — is expected to be closed when applying a reinterpretation of the null-results of the ATLAS R-hadron search for intermediate lifetimes. For instance, the ATLAS search in [81] performed for R-hadrons containing gluino bound states imposes limits down to a decay length of around 3 m that are similarly strong as in the detector-stable regime. The null-results in the CMS search for delayed jets [82] is expected to impose similar constraints for intermediate lifetimes, see e.g. [57] for a similar DM scenario.

Finally, we stress that the interplay of the above constraints is specific to the presence of the imposed Z_2 symmetry that renders DM absolutely stable. A variant of this model without a Z_2 symmetry has been studied, for instance, in [58, 59]. In general, allowing for a non-zero branching fraction of the mediator decay into standard model particles only, can lower the SW contribution to the DM density and, hence, relax the upper bound on the mediator mass found here. Furthermore, such a decay mode would change the LHC bounds. However, the requirement of a sufficiently long DM lifetime and indirect detection limits from DM decay provide additional constraints. A study of such scenarios is beyond the scope of this work.

5 Conclusions

Despite substantial experimental efforts dedicated to the search for DM, no indisputable signature of DM has been found in (astro-)particle physics experiments. As a complementary path to unveil the nature of DM, here we explored the imprint of non-cold DM, in the form of FIMPs, on cosmological observables. In particular, we provided generic lower bounds on the DM mass when DM is produced through the FI and SW mechanisms. Our FI bound is valid for FI via 2-body decays, and we discussed the applicability of this bound to the case of a production via $2 \to 2$ scatterings.

We first revisited the Boltzmann equations relevant for extracting the DM momentum distribution arising from these two production mechanisms and provided simple analytic

JCAP03(2022)041

expressions of these. Our results are given in eqs. (2.31). For FI we confirmed the result from previous literature, while the expression derived for the SW scenario — where DM arises from the late decay of a frozen-out mother particle — constitutes a new result. These analytic expressions can also be used to describe mixed FI-SW scenarios, where contributions from both FI and SW can be similarly important.

Due to their relatively large velocity dispersion at the time of structure formation, FIMPs from FI and SW production can affect clustering on small scales. Interestingly, the associated free-streaming effect can be constrained with Lyman-α forest data, as in the case of thermal WDM. For the purpose of exploiting this probe, we implemented the analytic DM momentum distribution for FI and SW in the Boltzmann code CLASS (which we will make publicly available). This allowed us to calculate the linear 3D matter power spectra and the corresponding transfer functions for both pure FI and SW DM production, as well as for mixed FI-SW scenarios where both contributions are relevant. In the case of pure FI and SW production, the transfer functions are similar in shape to the one of thermal WDM. This enabled us to provide generic fits to the transfer functions, the breaking scale of which depend on the DM model parameters: the DM mass, the mother particle mass, decay width, and the number of relativistic dof at the time of production, see eqs. (3.8) and (3.9). These novel results can be used to evaluate the effects of FIMP production on the linear matter power spectrum for the pure FI and SW scenarios, obviating the need to run a numerical Boltzmann code such as CLASS. For the mixed FI-SW scenario, however, the corresponding distribution and transfer function can significantly deviate from the thermal WDM case, requiring the numerical computation.

Usually to calculate general Lyman-α bounds on these NCDM models, one should run computationally expensive hydrodynamical simulations, in order to properly model the NCDM scenarios in the non-linear regime. Here we instead followed three alternative approaches to estimate the Lyman-α bound. The first one exploits the root mean square velocity of the DM particles today, while the second builds on the fits to the DM transfer functions that we provided and constrains the DM breaking scale. The third one makes use of the area criterion, which measures the suppression of the 1D NCDM matter power spectrum compared to the CDM one within the range of scales probed by the relevant cosmological experiments. After careful calibration checks on thermal WDM, see eqs. (3.7), (3.13) as well as appendix C, we reinterpreted the existing bound from Lyman-α forest observations on the WDM mass in terms of generic lower bounds on DM mass for pure FI and SW scenarios. Our results for each method are given in eq. (3.1) and table 1, assuming a lower bound on the thermal WDM mass given by $m_{\rm WDM}^{\rm Ly\alpha} = 5.3\,\text{keV}$. All three methods are in good agreement, which can be traced back to the fact that FI and SW production give rise to a cut in the matter power spectrum very similar to the one of thermal WDM. In the case of FI from 2-body decays, we recovered a lower bound on the DM mass of 15 keV (when $T_{\rm FI} > T_{\rm EW}$) in agreement with previous results, while the bound from SW could exclude much larger DM masses depending on the decay width and mass of mother particle. For mixed FI-SW scenarios, we reached the conclusion that the area criterion provides a conservative estimate of the DM mass bound.

When FIMPs arising from FI and SW are still relativistic at the time of BBN or CMB, they might provide a non negligible contribution to $\Delta N_{\rm eff}$. We obtained a generic lower bound on the DM mass of similar form as in the case of the Lyman-α bound. However, imposing $\Delta N_{\rm eff}(T_{\rm BBN}) < 0.31$, the resulting bound appears much looser, see table 1. Notice, though, that the latter bound can be applied without the need of using any Boltzmann code or hydrodynamical simulations and is also applicable in general to mixed scenarios, see eq. (3.19).

JCAP03(2022)041

Having seen the general application, we turned our attention to an example model, namely a coloured t-channel DM model. Here we revisited the top-philic DM model, taking special care in the treatment of non-perturbative effects, such as Sommerfeld and bound state enhancement effects on coloured mediator annihilation cross-section at early times, as well as on the computation of the DM production via $2 \to 2$ scatterings. This is of particular importance in this model in the case of SW and FI production, respectively. The two panels of figure 5 summarise the viable parameter space of FIMPs arising from FI and SW production in this scenario, complementarily bounded by cosmological (Lyman-α, BBN) and particle physics (LHC R-hadrons and displaced vertices searches) observables. In particular, the Lyman-α bound derived in the first part of this paper plays an important role. On the one hand, it excludes small DM masses, $\mathcal{O}(15\,\mathrm{keV})$, in the region of dominant FI production. On the other hand, it constrains the parameter space towards small couplings and, hence, large mediator lifetimes in the case of dominant SW production. In the latter case, Lyman-α observations supersede BBN constraints for mediator masses above $10^4\,\mathrm{GeV}$ and reach DM masses up to $\mathcal{O}(100\,\mathrm{GeV})$.

Here we have shown the importance of structure formation bounds in constraining FIMPs arising from FI and SW mechanisms, and illustrated the need to consider bounds from both particle physics and cosmology to fully understand these scenarios. In particular, the case of mixed NCDM models — giving rise to a multimodal momentum distribution — has, to our knowledge, not been discussed thoroughly in the literature. This case can naturally appear in FIMP scenarios with a decaying mother particle at the origin of the DM production. For the corresponding transfer function, which significantly deviates from the standard WDM scenario or from mixed warm + cold DM scenarios, no example hydrodynamical simulations have been run, and we can only provide a conservative lower bound on the DM mass. In future, it would be interesting to provide a thorough analysis of this case to validate our estimations and to check if other probes, such as reionization, the luminosity function at high redshift, or the 21 cm signal could help to test these models further and distinguish them from the WDM-like DM scenarios.

Acknowledgments

We would like to thank S. Junius for discussion and providing us with his recasting of DV+MET searches. We would also like to thank R. Murgia for clarifications on Lyman-α constraints for FIMPs as well as F. D'Eramo and A. Lenoci for discussions.

LLH is a Research associate and QD benefits form a FRIA PhD Grant of the Fonds de la Recherche Scientifique F.R.S.-FNRS. LLH, QD and DH acknowledge support of the FNRS research grant number F.4520.19 and the IISN convention 4.4503.15. JH acknowledges support from the Collaborative Research Center TRR 257 and the F.R.S.-FNRS (Chargé de recherches). DH is further supported by the Academy of Finland grant no. 328958.

A Details of the integration of the Boltzmann equations

In this section we highlight some parts of the calculations needed to solve the Boltzmann equation given in eq. (2.1) for the production of FIMPs from decays. First, we provide details on the derivation of the limits of integration in eq. (2.10). They arise from the fact that the cosine of the angle between the momenta of the decaying bath particle and the DM particle

JCAP03(2022)041

should satisfy the condition $|\cos\theta| \leq 1$ or, equivalently,

$$\left| \frac{m_A^2 - m_B^2 - m_\chi^2 + 2E_\chi E_B}{2p_B p} \right| \leq 1, \tag{A.1}$$

where p_B denotes the mother particle momentum and p is the DM momentum. This translates into the second order equation

$$4(p^2 - E_\chi^2)E_B^2 - 4E_\chi \Lambda\, E_B + \Lambda^2 + 4m_B^2 p^2 \leq 0\,, \tag{A.2}$$

with $\Lambda = m_B^2 + m_\chi^2 - m_A^2$. The two endpoints of this inequality yield the integration bounds $\xi_\pm$ in eq. (2.10). The generic form of these bounds, without neglecting m_χ, can be found in [30]. Assuming $m_\chi \ll m_B, m_A$, eq. (A.2) reduces to a first order equation, yielding only a lower bound on the rescaled energy of the bath particle in eq. (2.10),

$$\xi_B \geq \frac{q}{\delta} + \frac{\delta x^2}{4q} = \xi_{B\,\min}\,. \tag{A.3}$$

As a result, integrating eq. (2.6) over x between some $x_{\min}$ and x_0 we obtain

$$g_\chi f_\chi(q) = \int_{x_{\min}}^{x_0} \mathrm{d}x \frac{x^2 M_0}{16\pi m_B^3 q^2} \int_{\xi_{B\,\min}}^{\infty} \mathrm{d}\xi_B f_B |\mathcal{M}|^2_{B\to A\chi} \tag{A.4}$$

for FIMPs produced through B decay.

Below, we first further discuss the case for DM production via the FI process, and then the case of SW production.

Freeze-in from decays. In the case of FI, the FIMP is produced when the mother particle is in chemical and kinetic equilibrium with the bath. Assuming the Maxwell-Boltzmann distribution and setting the lower and upper integration bounds of x in eq. (A.4) to 0 and ∞, respectively, we obtain the analytic expression displayed in the main text, eq. (2.12).

Note that the lower limit of integration causes the resulting momentum distribution in eq. (2.12) to diverge for $q \to 0$. While this divergence does not affect the physically relevant quantities, such as the FIMP number density which involves the product $q^2 f_\chi(q)$, we stress that the divergence is absent altogether when the lower bound of the x integration, $x_{\min}$, is different from zero. In this latter case, the DM momentum distribution for production through freeze-in reads

$$g_\chi f_\chi^{\mathrm{FI,\,dec}}(q) = \frac{2g_B R_\Gamma^{\mathrm{FI}}}{\delta^3} \frac{\mathrm{e}^{-q}}{q} \left(x_{\min}\,\delta \exp\left[-\frac{x_{\min}^2\,\delta}{4q} \right] + \sqrt{\pi\delta q}\,\mathrm{erfc}\left[\frac{x_{\min}}{2}\sqrt{\frac{\delta}{q}} \right] \right), \tag{A.5}$$

where $\mathrm{erfc}(z)$ denotes the complementary error function. A realistic value of $x_{\min}$ corresponds to the reheating temperature, T_{rh}, with $x_{\min} \sim m_B/T_{\mathrm{rh}}$. The above approximation, $x_{\min} = 0$, is well justified as long as $T_{\mathrm{rh}} \gg m_B$.

SuperWIMP case for constant g_{*S}. In section 2.2.2, for SW production, i.e. after B has frozen out and has become non-relativistic, we consider for the equilibrium quantities

$$f_B^{\mathrm{eq}}(x,q) = \exp[-\sqrt{q^2+x^2}] \tag{A.6}$$

$$Y_B^{\mathrm{eq}}(x) = \frac{g_B}{g_{*S}} \frac{45}{2\pi^2} \left(\frac{x}{2\pi} \right)^{3/2} \exp[-x]\,, \tag{A.7}$$

JCAP03(2022)041

In the latter case, eq. (2.18) becomes:

$$g_\chi \partial_x f_\chi^{\rm SW}(x,q) = C_{\rm SW}\frac{\sqrt{x}}{q^2}\exp[x-\delta x^2/(4q)-q/\delta-R_\Gamma(x^2-x_{\rm FO}^2)/2]\,. \tag{A.8}$$

Integrating over x, we get a DM distribution function of the form

$$\begin{aligned} g_\chi f_\chi^{\rm SW} &= g_\chi\int_0^\infty {\rm d}x\,\partial_x f_\chi^{\rm SW}(x,q) \\ &= \frac{C_{\rm SW}}{\sqrt{2}q^{7/4}(\delta+2qR_\Gamma)^{5/4}}\exp\left(\frac{R_\Gamma x_{\rm FO}^2}{2}-\frac{q}{\delta}\right) \\ &\quad\times\left[q\,\Gamma\left(\frac{1}{4}\right){}_1F_1\left(\frac{5}{4},\frac{3}{2},\frac{q}{\delta+2qR_\Gamma}\right)+2\,\Gamma\left(\frac{3}{4}\right)\sqrt{q(\delta+2qR_\Gamma)}\,{}_1F_1\left(\frac{3}{4},\frac{1}{2},\frac{q}{\delta+2qR_\Gamma}\right)\right] \end{aligned} \tag{A.9}$$

where ${}_1F_1(a,b,z)$ is the Kummer confluent hypergeometric function. This result can be simplified to recover the solution given in eq. (2.19) in the following way. By setting the integration bounds of x to 0 and ∞, we make the approximation $x_{\rm FO}\simeq 0$, so we can drop the $x_{\rm FO}^2$ term in the resulting exponential.[17] In addition, we can expand the function ${}_1F_1(a,b,z)$ for large z, i.e. for $q\gg\delta+2qR_\Gamma$, to be:

$${}_1F_1(a,b,z)\simeq\frac{\Gamma(a)}{\Gamma(b)}z^{a-b}\exp(z) \tag{A.10}$$

to obtain:

$$g_\chi f_\chi^{\rm SW}\simeq\sqrt{8\pi}\,\frac{C_{\rm SW}}{q}\,\exp\left(-\frac{2q^2R_\Gamma}{\delta(2qR_\Gamma+\delta)}\right)\frac{1}{2qR_\Gamma+\delta} \tag{A.11}$$

Furthermore, assuming $2qR_\Gamma\ll\delta$ we arrive at the simple expression of eq. (2.19), which is the one we use in the bulk of the text in section 2.2.2.

SuperWIMP for varying $g_{*S}(x)$. When the number of relativistic dof vary in time while the FIMPs are produced, the choice of time and momentum variables in eq. (2.5) is not the most convenient. The total time derivative of eq. (2.1) would indeed involve two contributions:

$$\frac{{\rm d}f_\chi}{{\rm d}t}=x\bar{H}\partial_x f_\chi+\partial_t q\,\partial_q f_\chi\,, \tag{A.12}$$

with $\partial_t q=\partial_t g_{*S}^{1/3}\neq 0$ and $\bar{H}$ was defined in eq. (2.3). Trading T with $s^{1/3}$ and defining time and rescaled momentum variables:

$$x_s=\frac{m_{ref}}{s^{1/3}}\quad\text{and}\quad q_s=\frac{p}{s^{1/3}}\,, \tag{A.13}$$

we have in full generality:

$$x_s H\partial_{x_s}f_\chi=\mathcal{C}[f_\chi]\,, \tag{A.14}$$

[17] Similar to the case of freeze-in discussed above, setting the lower integration bound to 0 induces a formal divergence of $f_\chi(q)$ for $q\to 0$ that does, however, not affect the considered physically relevant quantities. Note that the contribution in eq. (A.9) from small x for which $Y_{\rm FO}\ll Y_B^{\rm eq}(x)$ is totally negligible in comparison to the contribution from freeze-in. This justifies the approximations made.

JCAP03(2022)041

as p and $s^{1/3}$ simply scale as $1/a$ when entropy is conserved, see also [33, 34] for similar choice of momentum variable. On general grounds, in eq. (A.14), we shall re-express all q and x variables in terms of q_s and x_s, we shall take into account the time-dependence of M_0[18]

$$\frac{\mathrm{d}\ln Y_B}{\mathrm{d}x_s} = -x_s R_\Gamma \frac{s^{2/3}}{T^2}\sqrt{\frac{g_*(x_s(T_{\rm SW}))}{g_*(x_s)}}\frac{K_1(x_s)}{K_2(x_s)} \tag{A.15}$$

where R_Γ is the constant factor of eq. (2.11), the ratio of $\sqrt{g_*}$ account for $M_0(x)$ dependence. We have also explicitly written the ratio of the modified Bessel functions of the second kind, which reduces to one in the non-relativistic limit, i.e. $x_s \gg 1$.

In this paper, we consider bath particles with masses above the TeV, i.e. with $T_{\rm FI} = m_B/3 > T_{\rm EW}$. In this case, the constant g_{*S} approach followed in the bulk of this paper is perfectly correct. In contrast, the SW decay could happen much latter and end up in a period with $g_{*S} \ll g_{*S}(T_{\rm EW})$. In the latter case, integrating out numerically eq. (A.14) from $x_s = x_s(T_{\rm FO})$ to ∞, one ends up with a momentum distribution $f_\chi(q_s)$ which in turn can be integrated out on q_s to obtain the correct DM relic number density. The variation of the number of relativistic dof along DM production could in particular affect the small coupling region of our viable parameter space of figure 5 where the SW mechanism drives the relic DM abundance. For the latter region, we have explicitly checked that, integrating numerically eq. (A.14), no significant change in the SW distribution function is observed compared to the analytic result derived with fixed value of the relativistic dof in section 2.2.2.

B Sommerfeld enhancement and bound state effects

In this appendix, we provide all expressions associated to Sommerfeld enhancement and bound state formation entering the computation of the effective annihilation cross-section, eq. (4.2). For a derivation of these expressions and further details we refer the reader to [28] and references therein.

In the Coulomb limit, the Sommerfeld enhancement factor for the s-wave annihilation process $\tilde{t}\tilde{t}^\dagger \to gg$ reads

$$S_{\rm Som} = \frac{2}{7}\,S_0\left(\frac{4\alpha_{\rm s}^{\rm S}}{3v_{\rm rel}}\right) + \frac{5}{7}\,S_0\left(-\frac{\alpha_{\rm s}^{\rm S}}{6v_{\rm rel}}\right) \tag{B.1}$$

where

$$S_0(\zeta) = \frac{2\pi\zeta}{1-e^{-2\pi\zeta}}\,. \tag{B.2}$$

Employing the non-relativistic limit, the thermally averaged bound state formation cross-section and ionization rate can be expressed as

$$\langle\sigma_{\tilde{t}\tilde{t}^\dagger\to\mathcal{B}g}v\rangle = \left(\frac{m_{\tilde{t}}}{T}\right)^{3/2}\left(\frac{1}{4\pi}\right)^{1/2}\int_0^\infty \mathrm{d}v_{\rm rel}\,v_{\rm rel}^2\,\exp\left(-\frac{m_{\tilde{t}}v_{\rm rel}^2}{4T}\right)\left[1+f_g(\omega)\right]\sigma_{\tilde{t}\tilde{t}^\dagger\to\mathcal{B}g}v_{\rm rel} \tag{B.3}$$

and

$$\Gamma_{\mathcal{B},\rm ion} = \frac{g_{\tilde{t}}^2 m_{\tilde{t}}^3}{16\pi^2 g_{\mathcal{B}}}\int_0^\infty \mathrm{d}v_{\rm rel}\,v_{\rm rel}^2\,f_g(\omega)\,\sigma_{\tilde{t}\tilde{t}^\dagger\to\mathcal{B}g}v_{\rm rel}\,, \tag{B.4}$$

[18] This allows us to rewrite $x\bar{H}\partial_x Y$ as $x_s H\partial_{x_s} Y$.

JCAP03(2022)041

respectively, where $g_{\tilde{t}} = 3$, $g_{\mathcal{B}} = 1$ and $f_g(\omega_g) = 1/(e^{\omega_g/T} - 1)$ is the gluon occupation number, with

$$\omega_g = \frac{m_{\tilde{t}}}{4}\left[\left(\frac{4\alpha_{\rm s}^{\rm B}}{3}\right)^2 + v_{\rm rel}^2\right] . \tag{B.5}$$

We consider the ground state only. The bound state formation cross-section appearing in the above expressions reads

$$\sigma_{\tilde{t}\tilde{t}^\dagger\to\mathcal{B}g} v_{\rm rel} = \frac{2^7 17^2}{3^5}\frac{\pi\alpha_{\rm s}^{\rm BSF}\alpha_{\rm s}^{\rm B}}{m_{\tilde{t}}^2} \times S_{\rm BSF}(\zeta_{\rm S}, \zeta_{\rm B}) , \tag{B.6}$$

where

$$S_{\rm BSF}(\zeta_{\rm S}, \zeta_{\rm B}) = S_0(\zeta_{\rm S})\,\frac{(1+\zeta_{\rm S}^2)\,\zeta_{\rm B}^4}{(1+\zeta_{\rm B}^2)^3}\,\exp\left[-4\,\zeta_{\rm S}\,{\rm acot}(\zeta_{\rm B})\right] , \tag{B.7}$$

and

$$\zeta_{\rm S} = -\frac{\alpha_{\rm s}^{\rm S}}{6 v_{\rm rel}} , \quad \zeta_{\rm B} = \frac{4\alpha_{\rm s}^{\rm B}}{3 v_{\rm rel}} . \tag{B.8}$$

Finally, the rate for the leading decay mode, $\mathcal{B} \to gg$, is

$$\Gamma_{\mathcal{B},{\rm dec}} = \frac{32}{81}\, m_{\tilde{t}}\, (\alpha_{\rm s}^{\rm ann})^2 (\alpha_{\rm s}^{\rm B})^3 . \tag{B.9}$$

The couplings $\alpha_{\rm s}^i$ in the above expressions denote the strong coupling, $\alpha_{\rm s} = g_s^2/(4\pi)$, evaluated at different scales:

$$\alpha_{\rm s}^{\rm ann} = \alpha_{\rm s}(m_{\tilde{t}}) , \quad \alpha_{\rm s}^{\rm S} = \alpha_{\rm s}\left(\frac{m_{\tilde{t}} v_{\rm rel}}{2}\right) , \quad \alpha_{\rm s}^{\rm B} = \alpha_{\rm s}\left(\frac{4 m_{\tilde{t}}\alpha_{\rm s}^{\rm B}}{6}\right) , \quad \alpha_{\rm s}^{\rm BSF} = \alpha_{\rm s}(\omega_g) . \tag{B.10}$$

C Lyman-α fit and fluid approximation

As discussed in section 3.1.2, [5] obtained a very good fit for α and μ (introduced in eq. (3.6)), from dedicated N-body simulations. In the aforementioned reference, for a given WDM mass $m_{\rm WDM}$, the best fit is obtained for $\mu = 1.12$ and

$$\alpha_{\rm WDM} = \alpha_{\rm prefactor}\left(\frac{m_{\rm WDM}}{1\,{\rm keV}}\right)^{-1.11}\left(\frac{\Omega_{\rm WDM}}{0.25}\right)^{0.11}\left(\frac{h}{0.7}\right)^{1.22} h^{-1}{\rm Mpc} , \tag{C.1}$$

with $\alpha_{\rm prefactor} = 0.049$. While this fit performs very well at masses of $m_{\rm WDM} \lesssim 3\,{\rm keV}$, which was more than enough given the existing bounds at the time the fit was derived, at higher WDM masses the accuracy degrades, leading to an error of a few percent. By comparing the fit to the transfer functions obtained from CLASS, we find the following adjustments:

$$\alpha_{\rm prefactor} = \begin{cases} 0.049 & \text{for } m_{\rm WDM} \lesssim 3\,{\rm keV} , \\ 0.045 & \text{for } 3\,{\rm keV} \lesssim m_{\rm WDM} \lesssim 6\,{\rm keV} , \\ 0.043 & \text{for } m_{\rm WDM} \gtrsim 6\,{\rm keV} . \end{cases} \tag{C.2}$$

We note that this prescription provides a very good fit to the thermal WDM transfer functions obtained with CLASS, provided that the perfect fluid approximation of the code is switched off. As discussed in [22], CLASS features a fluid approximation for NCDM models, whereby the species is treated as a perfect fluid, which allows to solve the Boltzmann hierarchy

JCAP03(2022)041

Parameter	FI		SW	
	Min	Max	Min	Max
m_χ [GeV]	1.4×10^{-5}	1.7×10^{-5}	1.0×10^{-1}	3.2×10^{2}
δ	0.5	1.0	0.5	1.0
$R_\Gamma^{\rm SW}$	—	—	7.0×10^{-17}	3.6×10^{-9}

Table 2. Parameter range for which the fits of eqs. (3.8) and (3.9) have been optimised.

quicker. This results in a substantial speed-up in the computation. However, as already discussed in [22], when considering smaller scales, such as those relevant for Lyman-α probes, this approximation needs to be turned off, which can be accomplished in CLASS by setting `ncdm_fluid_approximation = 3`. The validity of this approximation was also discussed recently in the context of other NCDM models, namely DM interacting with neutrinos, in [83].

As the fluid approximation needs to be turned off for improved accuracy, the computation of these models in CLASS is substantially slowed down. This is further hindered by the precise q-sampling needed in the phase-space distribution to properly account for both FI and SW contributions in the mixed scenarios. As such, obtaining the matter power spectrum for each model takes between 20–40 minutes, which, unfortunately, makes running Markov Chain Monte Carlo simulations infeasible. This justifies our choice to find alternative methods like those described in section 3.1.

Based on the fit obtained in eqs. (C.1) and (C.2), in section 3.1.2 we derived fits for pure FI and SW models (eqs. (3.8) and (3.9)). These fits have been optimised in the parameter range described in table 2.

References

[1] Planck collaboration, *Planck* 2018 *results. VI. Cosmological parameters*, *Astron. Astrophys.* **641** (2020) A6 [*Erratum ibid.* **652** (2021) C4] [arXiv:1807.06209] [INSPIRE].

[2] F. Kahlhoefer, *Review of LHC dark matter searches*, *Int. J. Mod. Phys. A* **32** (2017) 1730006 [arXiv:1702.02430] [INSPIRE].

[3] T. Marrodán Undagoitia and L. Rauch, *Dark matter direct-detection experiments*, *J. Phys. G* **43** (2016) 013001 [arXiv:1509.08767] [INSPIRE].

[4] J.M. Gaskins, *A review of indirect searches for particle dark matter*, *Contemp. Phys.* **57** (2016) 496 [arXiv:1604.00014] [INSPIRE].

[5] M. Viel, J. Lesgourgues, M.G. Haehnelt, S. Matarrese and A. Riotto, *Constraining warm dark matter candidates including sterile neutrinos and light gravitinos with WMAP and the Lyman-α forest*, *Phys. Rev. D* **71** (2005) 063534 [astro-ph/0501562] [INSPIRE].

[6] M. Viel, G.D. Becker, J.S. Bolton and M.G. Haehnelt, *Warm dark matter as a solution to the small scale crisis: new constraints from high redshift Lyman-α forest data*, *Phys. Rev. D* **88** (2013) 043502 [arXiv:1306.2314] [INSPIRE].

[7] N. Palanque-Delabrouille et al., *Hints, neutrino bounds and WDM constraints from SDSS DR*14 *Lyman-α and Planck full-survey data*, *JCAP* **04** (2020) 038 [arXiv:1911.09073] [INSPIRE].

[8] A. Garzilli, O. Ruchayskiy, A. Magalich and A. Boyarsky, *How warm is too warm? Towards robust Lyman-α forest bounds on warm dark matter*, arXiv:1912.09397 [INSPIRE].

JCAP03(2022)041

[9] S. Ikeuchi, *Galaxy formation theory and large scale structure in the universe*, in *Workshop on grand unified theories and cosmology*, (1986).

[10] M.J. Rees, *Lyman absorption lines in quasar spectra: evidence for gravitationally-confined gas in dark minihaloes*, *Mon. Not. Roy. Astron. Soc.* **218** (1986) 25P.

[11] V. Iršič et al., *New constraints on the free-streaming of warm dark matter from intermediate and small scale Lyman-α forest data*, *Phys. Rev. D* **96** (2017) 023522 [arXiv:1702.01764] [INSPIRE].

[12] M. Bolz, A. Brandenburg and W. Buchmüller, *Thermal production of gravitinos*, *Nucl. Phys. B* **606** (2001) 518 [*Erratum ibid.* **790** (2008) 336] [hep-ph/0012052] [INSPIRE].

[13] J. Pradler and F.D. Steffen, *Constraints on the reheating temperature in gravitino dark matter scenarios*, *Phys. Lett. B* **648** (2007) 224 [hep-ph/0612291] [INSPIRE].

[14] J. McDonald, *Thermally generated gauge singlet scalars as selfinteracting dark matter*, *Phys. Rev. Lett.* **88** (2002) 091304 [hep-ph/0106249] [INSPIRE].

[15] L. Covi, L. Roszkowski and M. Small, *Effects of squark processes on the axino CDM abundance*, *JHEP* **07** (2002) 023 [hep-ph/0206119] [INSPIRE].

[16] T. Asaka, K. Ishiwata and T. Moroi, *Right-handed sneutrino as cold dark matter*, *Phys. Rev. D* **73** (2006) 051301 [hep-ph/0512118] [INSPIRE].

[17] J.M. Frere, F.S. Ling, L. Lopez Honorez, E. Nezri, Q. Swillens and G. Vertongen, *MeV right-handed neutrinos and dark matter*, *Phys. Rev. D* **75** (2007) 085017 [hep-ph/0610240] [INSPIRE].

[18] L.J. Hall, K. Jedamzik, J. March-Russell and S.M. West, *Freeze-in production of FIMP dark matter*, *JHEP* **03** (2010) 080 [arXiv:0911.1120] [INSPIRE].

[19] L. Covi, J.E. Kim and L. Roszkowski, *Axinos as cold dark matter*, *Phys. Rev. Lett.* **82** (1999) 4180 [hep-ph/9905212] [INSPIRE].

[20] J.L. Feng, A. Rajaraman and F. Takayama, *SuperWIMP dark matter signals from the early universe*, *Phys. Rev. D* **68** (2003) 063504 [hep-ph/0306024] [INSPIRE].

[21] D. Blas, J. Lesgourgues and T. Tram, *The Cosmic Linear Anisotropy Solving System (CLASS) II: approximation schemes*, *JCAP* **07** (2011) 034 [arXiv:1104.2933] [INSPIRE].

[22] J. Lesgourgues and T. Tram, *The Cosmic Linear Anisotropy Solving System (CLASS) IV: efficient implementation of non-cold relics*, *JCAP* **09** (2011) 032 [arXiv:1104.2935] [INSPIRE].

[23] K.J. Bae, A. Kamada, S.P. Liew and K. Yanagi, *Light axinos from freeze-in: production processes, phase space distributions, and Ly-α forest constraints*, *JCAP* **01** (2018) 054 [arXiv:1707.06418] [INSPIRE].

[24] P. Bode, J.P. Ostriker and N. Turok, *Halo formation in warm dark matter models*, *Astrophys. J.* **556** (2001) 93 [astro-ph/0010389] [INSPIRE].

[25] R. Murgia, A. Merle, M. Viel, M. Totzauer and A. Schneider, *"Non-cold" dark matter at small scales: a general approach*, *JCAP* **11** (2017) 046 [arXiv:1704.07838] [INSPIRE].

[26] A. Schneider, *Astrophysical constraints on resonantly produced sterile neutrino dark matter*, *JCAP* **04** (2016) 059 [arXiv:1601.07553] [INSPIRE].

[27] M. Garny and J. Heisig, *Interplay of super-WIMP and freeze-in production of dark matter*, *Phys. Rev. D* **98** (2018) 095031 [arXiv:1809.10135] [INSPIRE].

[28] J. Harz and K. Petraki, *Radiative bound-state formation in unbroken perturbative non-Abelian theories and implications for dark matter*, *JHEP* **07** (2018) 096 [arXiv:1805.01200] [INSPIRE].

[29] J. Heeck and D. Teresi, *Cold keV dark matter from decays and scatterings*, *Phys. Rev. D* **96** (2017) 035018 [arXiv:1706.09909] [INSPIRE].

JCAP03(2022)041

[30] S. Boulebnane, J. Heeck, A. Nguyen and D. Teresi, *Cold light dark matter in extended seesaw models*, *JCAP* **04** (2018) 006 [arXiv:1709.07283] [INSPIRE].

[31] G. Ballesteros, M.A.G. Garcia and M. Pierre, *How warm are non-thermal relics? Lyman-α bounds on out-of-equilibrium dark matter*, *JCAP* **03** (2021) 101 [arXiv:2011.13458] [INSPIRE].

[32] F. D'Eramo and A. Lenoci, *Lower mass bounds on FIMP dark matter produced via freeze-in*, *JCAP* **10** (2021) 045 [arXiv:2012.01446] [INSPIRE].

[33] G. Bélanger, F. Boudjema, A. Goudelis, A. Pukhov and B. Zaldivar, *MicrOMEGAs*5.0*: freeze-in*, *Comput. Phys. Commun.* **231** (2018) 173 [arXiv:1801.03509] [INSPIRE].

[34] G. Bélanger, C. Delaunay, A. Pukhov and B. Zaldivar, *Dark matter abundance from the sequential freeze-in mechanism*, *Phys. Rev. D* **102** (2020) 035017 [arXiv:2005.06294] [INSPIRE].

[35] T. Binder, T. Bringmann, M. Gustafsson and A. Hryczuk, *Early kinetic decoupling of dark matter: when the standard way of calculating the thermal relic density fails*, *Phys. Rev. D* **96** (2017) 115010 [*Erratum ibid.* **101** (2020) 099901] [arXiv:1706.07433] [INSPIRE].

[36] P. Gondolo and G. Gelmini, *Cosmic abundances of stable particles: improved analysis*, *Nucl. Phys. B* **360** (1991) 145 [INSPIRE].

[37] I. Baldes, Q. Decant, D.C. Hooper and L. Lopez-Honorez, *Non-cold dark matter from primordial black hole evaporation*, *JCAP* **08** (2020) 045 [arXiv:2004.14773] [INSPIRE].

[38] A. Merle and M. Totzauer, *keV sterile neutrino dark matter from singlet scalar decays: basic concepts and subtle features*, *JCAP* **06** (2015) 011 [arXiv:1502.01011] [INSPIRE].

[39] S. Baumholzer, V. Brdar, P. Schwaller and A. Segner, *Shining light on the scotogenic model: interplay of colliders and cosmology*, *JHEP* **09** (2020) 136 [arXiv:1912.08215] [INSPIRE].

[40] C. Dvorkin, T. Lin and K. Schutz, *Making dark matter out of light: freeze-in from plasma effects*, *Phys. Rev. D* **99** (2019) 115009 [arXiv:1902.08623] [INSPIRE].

[41] C. Dvorkin, T. Lin and K. Schutz, *Cosmology of sub-MeV dark matter freeze-in*, *Phys. Rev. Lett.* **127** (2021) 111301 [arXiv:2011.08186] [INSPIRE].

[42] S. Ikeuchi, *The baryon clump within an extended dark matter region*, *Astrophys. Space Sci.* **118** (1986) 509.

[43] S. Colombi, S. Dodelson and L.M. Widrow, *Large scale structure tests of warm dark matter*, *Astrophys. J.* **458** (1996) 1 [astro-ph/9505029] [INSPIRE].

[44] K. Jedamzik, M. Lemoine and G. Moultaka, *Gravitino, axino, Kaluza-Klein graviton warm and mixed dark matter and reionisation*, *JCAP* **07** (2006) 010 [astro-ph/0508141] [INSPIRE].

[45] J. Baur et al., *Constraints from Ly-α forests on non-thermal dark matter including resonantly-produced sterile neutrinos*, *JCAP* **12** (2017) 013 [arXiv:1706.03118] [INSPIRE].

[46] R. Murgia, V. Iršič and M. Viel, *Novel constraints on noncold, nonthermal dark matter from Lyman-α forest data*, *Phys. Rev. D* **98** (2018) 083540 [arXiv:1806.08371] [INSPIRE].

[47] M. Archidiacono, D.C. Hooper, R. Murgia, S. Bohr, J. Lesgourgues and M. Viel, *Constraining dark matter-dark radiation interactions with CMB, BAO, and Lyman-α*, *JCAP* **10** (2019) 055 [arXiv:1907.01496] [INSPIRE].

[48] D. Egana-Ugrinovic, R. Essig, D. Gift and M. LoVerde, *The cosmological evolution of self-interacting dark matter*, *JCAP* **05** (2021) 013 [arXiv:2102.06215] [INSPIRE].

[49] R. Murgia, *Constraining dark matter properties with the inter-galactic medium and other probes*, Ph.D. thesis, SISSA, Trieste, Italy (2019).

[50] M. Hufnagel, K. Schmidt-Hoberg and S. Wild, *BBN constraints on MeV-scale dark sectors. Part I. Sterile decays*, *JCAP* **02** (2018) 044 [arXiv:1712.03972] [INSPIRE].

JCAP03(2022)041

[51] C. Pitrou, A. Coc, J.-P. Uzan and E. Vangioni, *Precision big bang nucleosynthesis with improved helium-4 predictions*, *Phys. Rept.* **754** (2018) 1 [arXiv:1801.08023] [INSPIRE].

[52] PARTICLE DATA GROUP collaboration, *Review of particle physics*, *Chin. Phys. C* **40** (2016) 100001 [INSPIRE].

[53] S.-P. Li, X.-Q. Li, X.-S. Yan and Y.-D. Yang, *Simple estimate of BBN sensitivity to light freeze-in dark matter*, *Phys. Rev. D* **104** (2021) 115007 [arXiv:2106.07122] [INSPIRE].

[54] G. Bélanger, F. Boudjema, C. Hugonie, A. Pukhov and A. Semenov, *Relic density of dark matter in the NMSSM*, *JCAP* **09** (2005) 001 [hep-ph/0505142] [INSPIRE].

[55] A. Ibarra, A. Ringwald and C. Weniger, *Hidden gauginos of an unbroken* U(1)*: Cosmological constraints and phenomenological prospects*, *JCAP* **01** (2009) 003 [arXiv:0809.3196] [INSPIRE].

[56] G. Bélanger et al., *LHC-friendly minimal freeze-in models*, *JHEP* **02** (2019) 186 [arXiv:1811.05478] [INSPIRE].

[57] L. Calibbi, F. D'Eramo, S. Junius, L. Lopez-Honorez and A. Mariotti, *Displaced new physics at colliders and the early universe before its first second*, *JHEP* **05** (2021) 234 [arXiv:2102.06221] [INSPIRE].

[58] G. Arcadi and L. Covi, *Minimal decaying dark matter and the LHC*, *JCAP* **08** (2013) 005 [arXiv:1305.6587] [INSPIRE].

[59] G. Arcadi, L. Covi and F. Dradi, *LHC prospects for minimal decaying dark matter*, *JCAP* **10** (2014) 063 [arXiv:1408.1005] [INSPIRE].

[60] A. Ibarra, A. Pierce, N.R. Shah and S. Vogl, *Anatomy of coannihilation with a scalar top partner*, *Phys. Rev. D* **91** (2015) 095018 [arXiv:1501.03164] [INSPIRE].

[61] M. Garny, J. Heisig, M. Hufnagel and B. Lülf, *Top-philic dark matter within and beyond the WIMP paradigm*, *Phys. Rev. D* **97** (2018) 075002 [arXiv:1802.00814] [INSPIRE].

[62] A. Sommerfeld, *Über die Beugung und Bremsung der Elektronen* (in German), *Annalen Phys.* **403** (1931) 257.

[63] J. Hisano, S. Matsumoto and M.M. Nojiri, *Unitarity and higher order corrections in neutralino dark matter annihilation into two photons*, *Phys. Rev. D* **67** (2003) 075014 [hep-ph/0212022] [INSPIRE].

[64] M. Cirelli, A. Strumia and M. Tamburini, *Cosmology and astrophysics of minimal dark matter*, *Nucl. Phys. B* **787** (2007) 152 [arXiv:0706.4071] [INSPIRE].

[65] S.P. Liew and F. Luo, *Effects of QCD bound states on dark matter relic abundance*, *JHEP* **02** (2017) 091 [arXiv:1611.08133] [INSPIRE].

[66] A. Mitridate, M. Redi, J. Smirnov and A. Strumia, *Cosmological implications of dark matter bound states*, *JCAP* **05** (2017) 006 [arXiv:1702.01141] [INSPIRE].

[67] S. Biondini and M. Laine, *Thermal dark matter co-annihilating with a strongly interacting scalar*, *JHEP* **04** (2018) 072 [arXiv:1801.05821] [INSPIRE].

[68] F. Ambrogi et al., *MadDM v.*3.0*: a comprehensive tool for dark matter studies*, *Phys. Dark Univ.* **24** (2019) 100249 [arXiv:1804.00044] [INSPIRE].

[69] T. Binder, *Refining the chemical and kinetic decoupling description of thermally produced dark matter*, Ph.D. thesis, Gottingen U., Gottingen, Germany (2019).

[70] S. Biondini and J. Ghiglieri, *Freeze-in produced dark matter in the ultra-relativistic regime*, *JCAP* **03** (2021) 075 [arXiv:2012.09083] [INSPIRE].

[71] G. Jackson and M. Laine, *Efficient numerical integration of thermal interaction rates*, *JHEP* **09** (2021) 125 [arXiv:2107.07132] [INSPIRE].

JCAP03(2022)041

[72] ATLAS collaboration, *Search for heavy charged long-lived particles in the ATLAS detector in 36.1 fb^{-1} of proton-proton collision data at $\sqrt{s} = 13$ TeV*, *Phys. Rev. D* **99** (2019) 092007 [arXiv:1902.01636] [INSPIRE].

[73] ATLAS collaboration, *Search for long-lived, massive particles in events with displaced vertices and missing transverse momentum in $\sqrt{s} = 13$ TeV pp collisions with the ATLAS detector*, *Phys. Rev. D* **97** (2018) 052012 [arXiv:1710.04901] [INSPIRE].

[74] W. Beenakker, C. Borschensky, M. Krämer, A. Kulesza and E. Laenen, *NNLL-fast: predictions for coloured supersymmetric particle production at the LHC with threshold and Coulomb resummation*, *JHEP* **12** (2016) 133 [arXiv:1607.07741] [INSPIRE].

[75] K. Jedamzik, *Big bang nucleosynthesis constraints on hadronically and electromagnetically decaying relic neutral particles*, *Phys. Rev. D* **74** (2006) 103509 [hep-ph/0604251] [INSPIRE].

[76] M. Kawasaki, K. Kohri, T. Moroi and Y. Takaesu, *Revisiting big-bang nucleosynthesis constraints on long-lived decaying particles*, *Phys. Rev. D* **97** (2018) 023502 [arXiv:1709.01211] [INSPIRE].

[77] K. Jedamzik, *Bounds on long-lived charged massive particles from big bang nucleosynthesis*, *JCAP* **03** (2008) 008 [arXiv:0710.5153] [INSPIRE].

[78] M. Kusakabe, T. Kajino, T. Yoshida and G.J. Mathews, *Effect of long-lived strongly interacting relic particles on big bang nucleosynthesis*, *Phys. Rev. D* **80** (2009) 103501 [arXiv:0906.3516] [INSPIRE].

[79] P.F. Depta, M. Hufnagel and K. Schmidt-Hoberg, *ACROPOLIS: A generiC fRamework fOr Photodisintegration Of LIght elementS*, *JCAP* **03** (2021) 061 [arXiv:2011.06518] [INSPIRE].

[80] A. Arbey, *AlterBBN: a program for calculating the BBN abundances of the elements in alternative cosmologies*, *Comput. Phys. Commun.* **183** (2012) 1822 [arXiv:1106.1363] [INSPIRE].

[81] ATLAS collaboration, *Search for heavy charged long-lived particles in proton-proton collisions at $\sqrt{s} = 13$ TeV using an ionisation measurement with the ATLAS detector*, *Phys. Lett. B* **788** (2019) 96 [arXiv:1808.04095] [INSPIRE].

[82] CMS collaboration, *Search for long-lived particles using nonprompt jets and missing transverse momentum with proton-proton collisions at $\sqrt{s} = 13$ TeV*, *Phys. Lett. B* **797** (2019) 134876 [arXiv:1906.06441] [INSPIRE].

[83] M.R. Mosbech, C. Boehm, S. Hannestad, O. Mena, J. Stadler and Y.Y.Y. Wong, *The full Boltzmann hierarchy for dark matter-massive neutrino interactions*, *JCAP* **03** (2021) 066 [arXiv:2011.04206] [INSPIRE].

JCAP03(2022)041